Research Papers

Analysis of the improvement of a lithium-ion battery module cooling system employing nanofluid and nano encapsulated phase change materials by means of a lumped electro-thermal model

Antonio José Torregrosa, Alberto Broatch, Pablo Olmeda [*], Luca Agizza

CMT – Motores Térmicos, Universitat Politècnica de València, Camino de Vera s/n, 46022, Valencia, Spain

A B S T R A C T

In this study an analysis of the employment of nanoparticles and nano encapsulated phase change materials for battery cooling is provided. By using a previously validated electro-thermal model of a lithium-ion battery module, the effect of 5 different nanoparticles and 6 different nano encapsulated phase change materials is estimated. The analysis is provided for a battery module charge process at 4C, with a coolant mass flow of 2 l/min and with ambient and fluid temperature equal to 20 °C. The concentration of the nanofluid is varied between 0.01 % and 5 %. By increasing the concentration, a beneficial effect is observed on the battery cooling, in terms of maximum temperature achieved during the charge process and heat dissipated into the coolant. Among the 30 different combinations of nanoparticles and nano encapsulated phase change materials analyzed in this work, it is concluded that the best results in terms of dissipated heat and maximum temperature are obtained for copper oxide (CuO) combined with octadecane. In this case, at 20 °C, a reduction of the maximum temperature of about 2 °C is obtained with a volume fraction equal to 5 %, with respect to the case in which there are no nanoparticles. Furthermore, the total heat dissipated in the coolant is increased by 28 %. Finally, the study proposes a design of experiment to evaluate the performance of a phase change material for battery cooling. For this analysis, 4 variables are considered (concentration, melting temperature, heat of fusion and characteristic temperature range) and the effect on the maximum temperature and on the temperature spatial difference is observed: it is found that the thermal evolution of the cells is mostly affected by melting temperature and concentration.

1. Introduction

The recent developments in the European policies are pushing the automotive industry towards a transition from traditional powertrains to electrified ones [1]. The ban of the internal combustion engine vehicles (ICEV) starting from 2035 is only the last of a series of decisions in this direction [2]. The cost of the electric vehicle has increasingly decreased in the last decade, due to a quick spread of the vehicles among the consumers and due to a better understanding and comprehension of the electric vehicles related issues [3]. The lithium-ion battery is the component which is affected by the most critical issues in an electrified vehicle. In particular, the thermal issues have been focusing of lots of studies in literature to find different strategies to keep battery temperature within an optimal temperature range [4]. A lithium-ion battery can work properly only in a limited range of temperatures between 15 °C and 35 °C [5]. For lower temperatures, some issues can appear as the

formation of lithium dendrites and the lithium plating: these phenomena limit the capacity of the battery, and they can also provoke very dangerous situations such as short circuits [6]. On the other hand, when the temperatures increase, some phenomena start to happen inside the cell, such as solid electrolyte interface decomposition, cathode oxygen release, separator short circuit and finally thermal runaway, that can bring to very dangerous situations such as venting and fire of the cell [7]. Therefore, a big effort has been done to develop thermal management systems which could keep the cells temperature within this safety operational window [8]. The most common thermal management system for battery are air cooling systems or liquid cooling systems [9]. The liquid cooling systems could be divided into 2 categories [10]: the direct liquid cooling system, where the battery is in direct contact with a cooling liquid, that is a dielectric coolant, which is characterized by very high electric resistivity, but also very good thermal conductivity [11]; the other category is the indirect liquid cooling in which a coolant flows

Fig. 1. First order equivalent circuit model.

Table 1
32,700 cylindrical lithium-ion cell.

Nominal capacity	6 Ah
Nominal voltage	3.2 V
Maximum voltage	3.65 V
Minimum voltage	2 V
Diameter	32 mm
Length	70 mm
Cathode/anode chemistry	LFP/graphite
Discharge temperature	[−10 60] °C
Charge temperature	[0 45] °C

Table 2
Battery tester precision and resolution.

Voltage resolution	~1 µV
Voltage control accuracy	±2 mV
Current control accuracy	±20 mA

Table 3
Climatic chamber characteristics.

Temperature range	[−75,180] °C
Temperature fluctuation in time	<0.3 K
Temperature variation in space	<3.0 K
Heat up rate	4.7 K/min
Pull-down rate	4.1 K/min
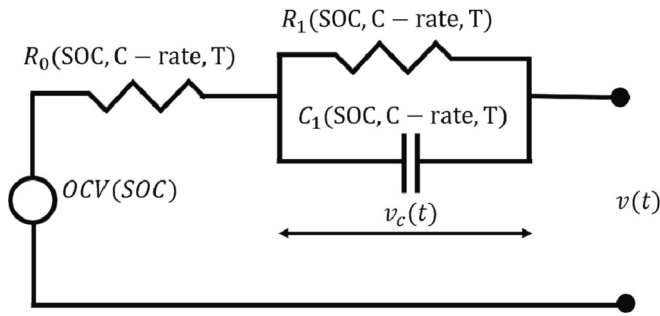
through a plate which can be a serpentine one, like in the Tesla's batteries or a flat one like in Lucid Motors' batteries [12]. Usually, an ethylene glycol water solution is used as a coolant in a battery pack [13]. Nonetheless, other types of coolant have been tried for lithium-ion battery cooling applications: synthetic hydrocarbons of aromatic chemistry, for example diethyl benzene [14]; aliphatic hydrocarbons of paraffinic and iso-paraffinic type [15]; silicone oils [16]; fluorocarbons such as perfluorocarbons, hydrofluoethers and perfluorocarbon ethers [17]; liquid metals of Ga-In-Sn chemistry [18]. Finally, to improve characteristics of the initial coolant, suspensions of nanoparticles have been tried [19]. A nanofluid is, in fact, a coolant such as ethylene glycol water solution, to which a certain concentration of a nanoparticle has been added. Several types of nanofluid have been proposed for lithium-ion battery cooling purposes. They can be gathered into three categories [20]: ceramic nanofluids, such as copper oxide nanofluids, aluminum oxide nanofluids, titanium dioxide nanofluids and zinc oxide nanofluids; magnetic nanofluid such as Co and Fe oxides; metallic nanofluids such as dispersed copper particles into a solution. Ceramic nanofluids have been found particularly suitable to this kind of applications due to their stability in solution, resistance to oxidation and low density. In the literature, several works have analyzed thermal management systems of lithium-ion batteries employing nanoparticles. Sefidan et al. [21]

analyzed the impact of aluminum oxide nanoparticles on the cooling of a commercial 18,650 lithium-ion battery by means of a pseudo 2D electrochemical model. They considered discharge processes of the battery module at 1C, 2C and 3C: among their finding, a better uniformity of the temperature in the battery module and a reduction of the maximum temperature during the discharge process is found using nanofluids. Tousi et al. [22] proposed a novel battery thermal management system based on AgO nanofluid, aimed to keep maximum temperature and temperature homogeneousness within the optimal ranges. The authors analyzed the impact of the discharge rate, of the volumetric fraction of nanofluid and of the inflow velocity on the thermal efficiency of the
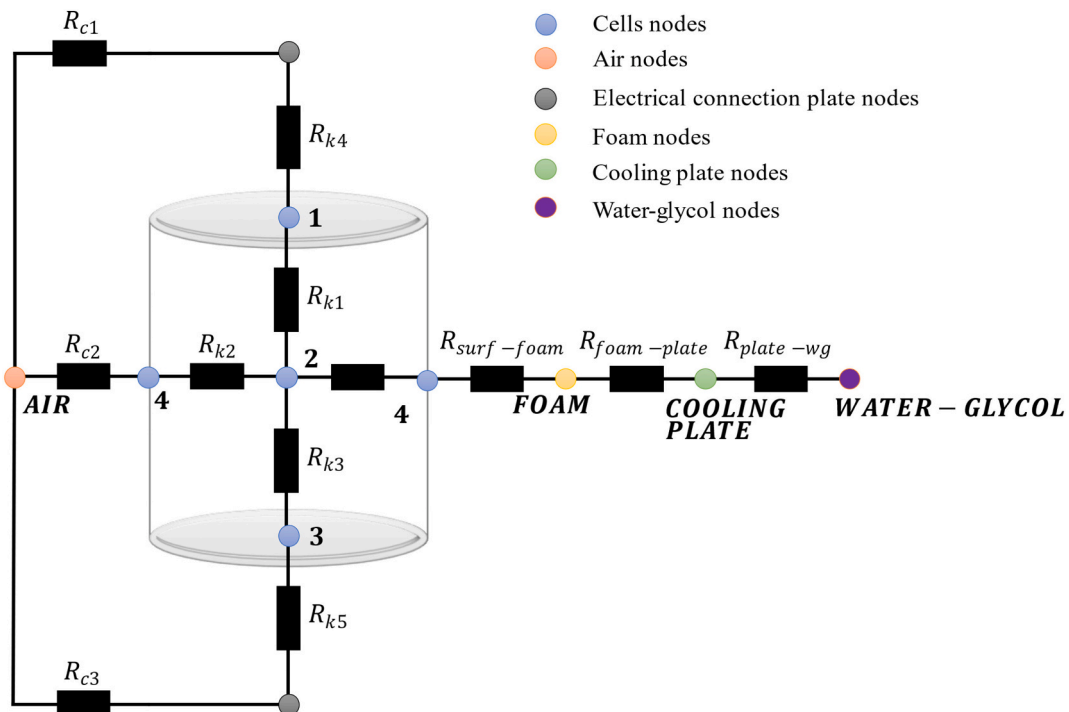

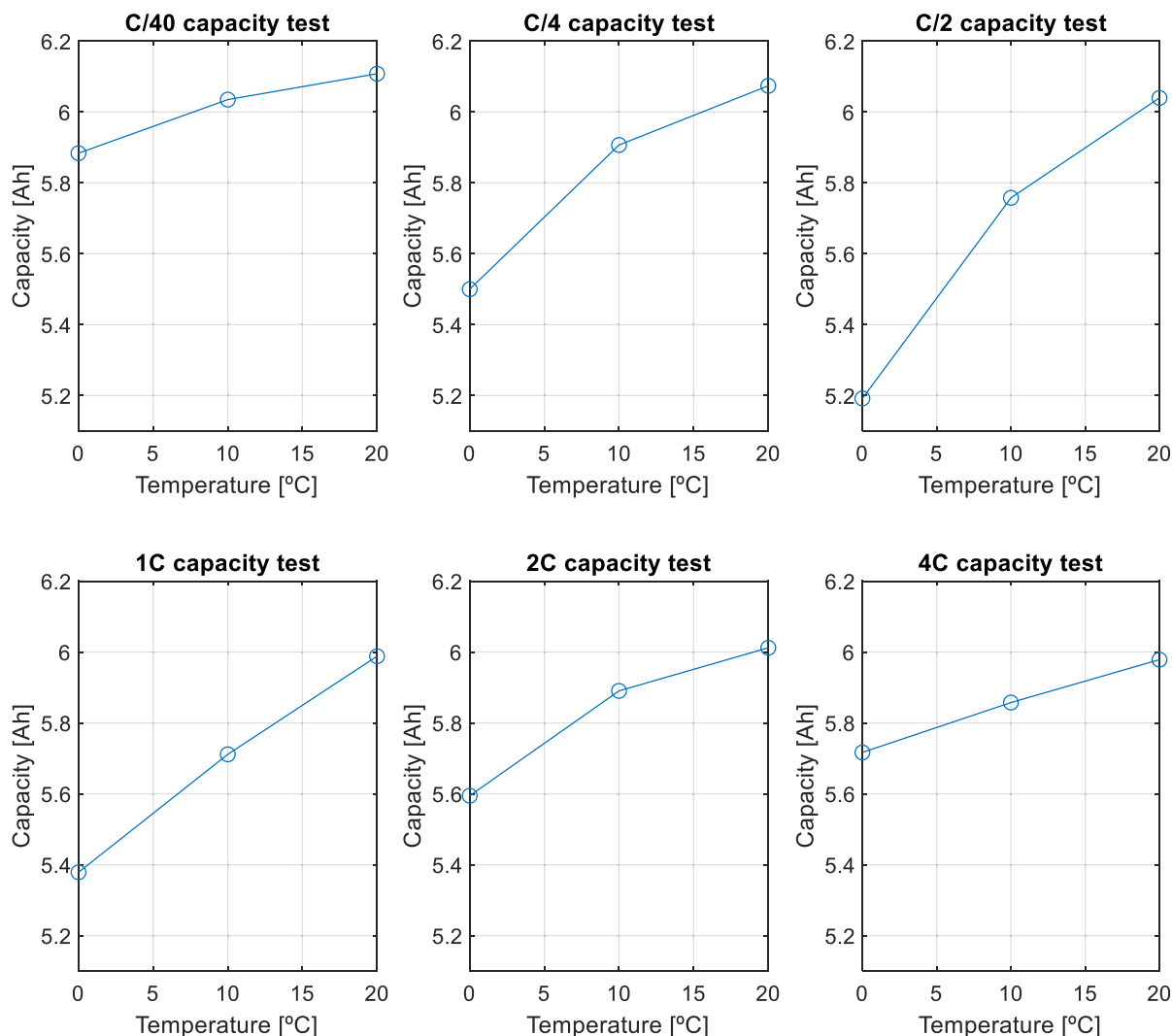**Fig. 2.** Nodal network of one cell for module nodal network.

Fig. 3. Capacity test results.

battery pack by means of a computational fluid dynamics (CFD) model. They found out that the maximum temperature and temperature difference decreased with the increase of the inflow velocity and of the volumetric fluid fraction. Mondal et al. [23] studied the use of nanofluids in a base fluid by means of a electrochemical-thermal model. They analyzed the impact of aluminum oxide on the thermal efficiency of a battery module composed by twenty prismatic cells. This battery module was discharged at several c-rates and maximum temperature and the temperature difference in the module was analyzed. The authors found that the addition of nanoparticles, in this case, did not have a meaningful impact on the module temperature: this is because adding nanoparticles to the initial fluid leads to a decrease of the heat capacity. Sarchami et al. [24] propose a numerical analysis of an innovative liquid cooling system employing aluminum oxide nanofluid. They used a three-dimensional (3D) model to model the battery module and its thermal management system. Among their findings, the authors concluded that the addition of the aluminum oxide with a 2 % volume fraction meaningfully reduces the maximum temperature and the spatial temperature difference inside the battery module. Nasir et al. [25] analyze a thermal management system employing aluminum oxide by means of a CFD model. The authors found that by using a 1.5 % of concentration of the nanoparticle, the total thermal resistance could be reduced by as much as 15 %.

Nonetheless the use of nanofluids notably increases the thermal conductivity of the fluid, on the other hand, there is a drawback which must be considered, that is the reduction of the thermal heat capacity. As Torregrosa et al. [26] found in their study, the addition of nano encapsulated phase change material (NePCM) to the nanoparticle can overcome this limitation: in their model, when the temperature of the fluid achieves the melting temperature of the NePCM, the heat capacity of the fluid increases due to the term depending on the heat of fusion of the phase change. Cao et al. [27] proposed a lithium-ion battery cooling system employing a n-nonadecane with a fusion temperature of 30.44 °C. The authors found that increasing of Reynolds number from 70 to 100 improved the thermal efficiency of the lithium-ion battery cooling system in terms of heat transfer rate. Also, the increase of the volume fraction leads to higher values of the heat transfer rate. Qaderi et al. [28] analyzed the performance of battery thermal management system employing a NePCM. They found out that the closer to the melting temperature of the NePCM the ambient temperature is, the more efficient the thermal management system is. Gu et al. [29] evaluated the impact of NePCMs on a battery thermal management system. Among their outcomes, they found an increase of the thermal conductivity by 49 % and a decrease of the maximum battery temperature of 3.95 °C compared to the base case realized without the addition of NePCMs particles. Huang et al. [30] analyzed a paraffin, as a phase change material and its impact on a lithium-ion battery module. They found that,
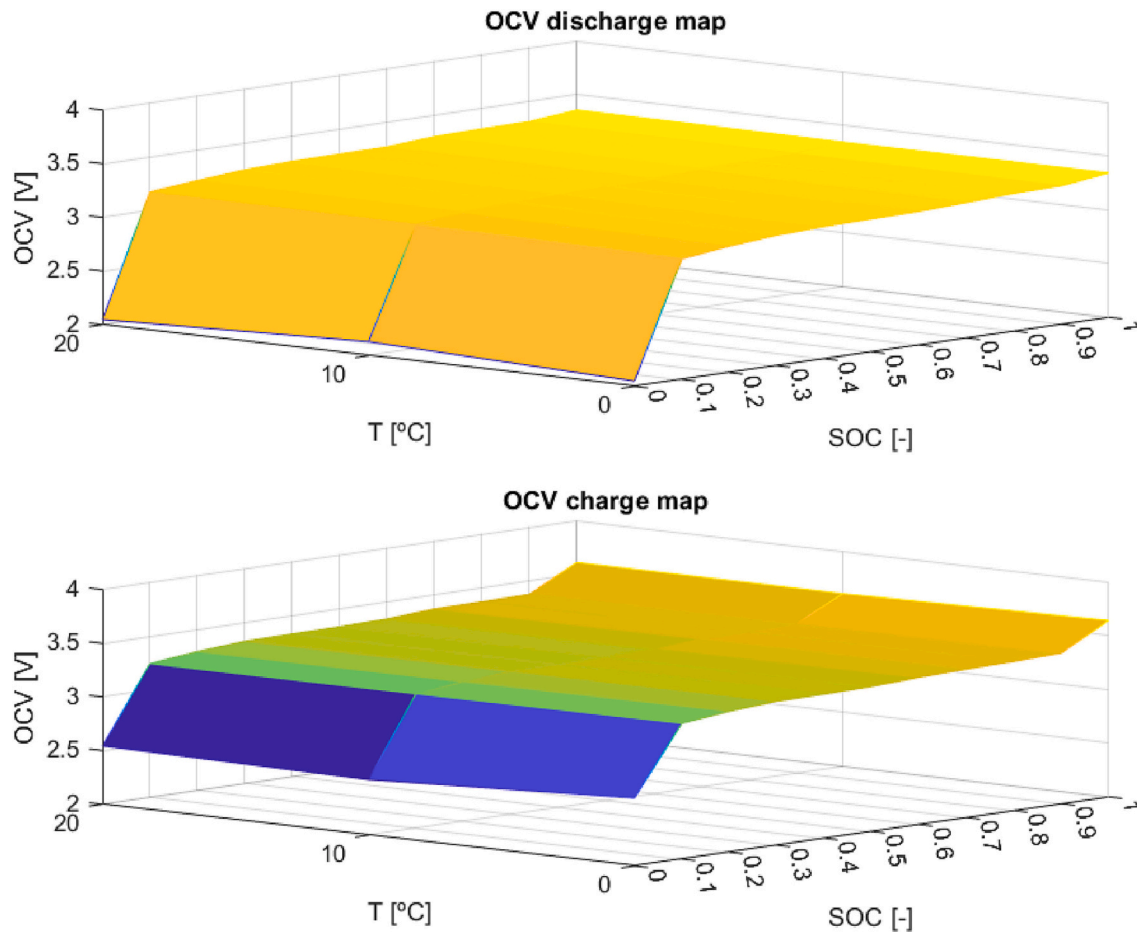
Fig. 4. Open circuit voltage test results.

during a 5C discharge process, employing the paraffin, the maximum temperature could be kept below 46 °C and the temperature difference could be kept within 4 °C.

In this work the authors propose an analysis of different combinations of nanoparticles and nano encapsulated phase change materials by means of a previously validated lumped electro-thermal model. The main novelties of this work are listed below:

- A benchmark of several combinations of nanoparticles and phase change materials for a lithium-ion battery cooling is performed. For this purpose, a high-fidelity reduced order model composed by a reliable link between an equivalent circuit model and a thermal lumped model of cells and the rest of elements of the cooling system is used.
- The identification of the NePCM characteristics which have the biggest impact on the thermal evolution of the battery module by means of a statistical approach.

Finally this work is composed by the following sections: Section 2 is the introduction; Section 3 is about cell electro-thermal model development and validation; Section 4 is about battery module model and nanofluid thermo-physical properties calculation; Section 5 is about the effects of the nanofluid on heat transfer coefficient; Section 6 is about the results of the analysis for the 30 different combinations of nanofluid and NePCMs; Section 7 shows the results of the design of experiment; Section 8 is about the conclusions of the work.

Nomenclature

c_i	specific heat of ith node, $J \bullet kg^{-1}K^{-1}$
C_{Ah}	measured capacity, Ah
C_1	double layer capacitance, F
D	Hydraulic diameter, m
f	Friction coefficient
h	Heat transfer, $W \bullet m^{-2}K^{-1}$
h_{ij}	Heat transfer between ith node and fluid, $W \bullet m^{-2}K^{-1}$
H_{NePCM}	Heat of fusion for the change of phase, $J \bullet kg^{-1}$
$H_{dissipated}$	Total heat dissipated into the coolant, J
I	electrical current, A
k	Thermal conductivity, $W \bullet m^{-1}K^{-1}$
L	Characteristic length of the system
m_i	mass of ith node, kg
Nu	Nusselt number
ΔP	pressure drop, bar
$\dot{Q}_g$	Heat generated by the cells, W
$\dot{Q}_{k \rightarrow i}$	heat generation source inside control volume of the node, W
Pr	Prandtl number
R_0	ohmic resistance, Ω
R_1	charge transfer resistance, Ω
T_{fluid}	fluid node temperature, K
T_{fusion}	melting temperature, K
$T_{t+\Delta t}^{i}$	temperature of ith node at $t + \Delta t$ instant, K
T_t^i	temperature of ith node at t instant, K
T	temperature, K

T_{MAX}	Maximum temperature in the battery module, K
ΔT	Characteristic temperature width, K
ΔT_{cells}	Spatial temperature difference in the battery module, K
t_0	initial time, s
t	time, s
u	Fluid velocity, m/s
v_c	voltage at RC branch, V
v	terminal voltage, V
$\dot{V}$	Volumetric flow, m^3/s
$\dot{W}$	Power consumed by the pump, W

Subscripts

b	base fluid
l	nanolayer
nf	nanofluid
p	nanoparticle

Greek letters

β	ratio of nanolayer thickness to the nanoparticle radius
γ	ratio of nanolayer thermal conductivity divided by nanoparticle thermal conductivity
δ	nanolayer thickness
μ	dynamic viscosity, m^2/s
ρ	density, kg/m^3
φ	volumetric fraction, %

Acronyms

BMS	Battery management system
CCCV	Constant Current Constant Voltage
CFD	Computational Fluid Dynamics
DOE	Design of experiment
ECM	Equivalent Circuit Model
HPPC	Hybrid Pulse Power Characterization
LFP	Lithium iron phosphate
NePCM	Nano encapsulated phase change material
OCV	Open circuit voltage
RMSE	Root Mean Square Error
SOC	State of charge

2. Cell electro-thermal model

In this work a lumped electro-thermal model for the description of cell behavior has been employed. In this section, a description of both the electric and thermal models is provided, as well as the description of the experimental set-up and the characterization campaign carried out to determine models' parameters. Finally, a validation of the model at cell level is provided in a very dynamic condition.

2.1. Lumped electro-thermal model

The model employed for this analysis is composed by an equivalent circuit model and a thermal nodal network to represent, respectively, the electric and thermal dynamic of a lithium-ion cell. In comparison with CFD or electrochemical models' approach, this model is
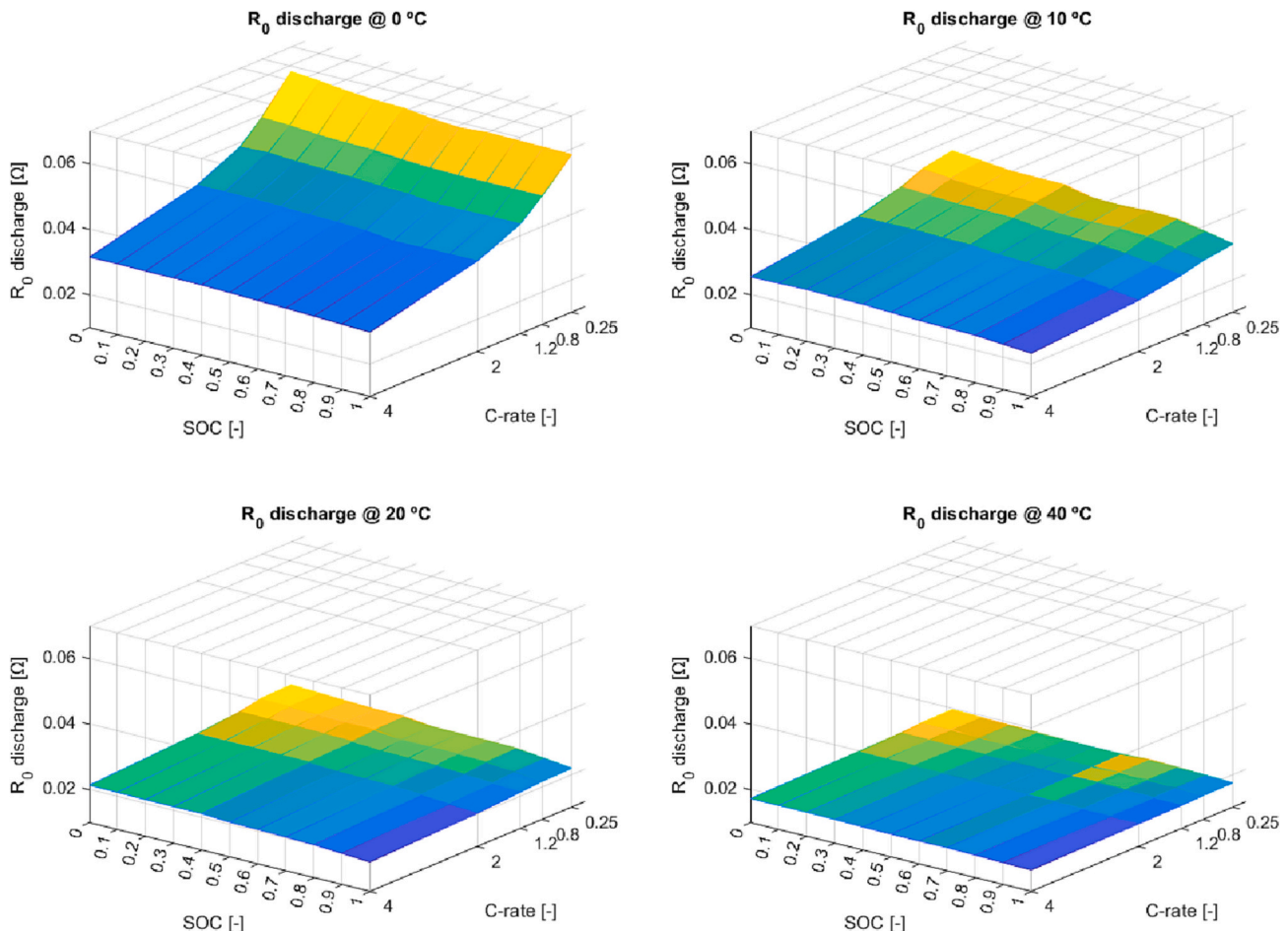

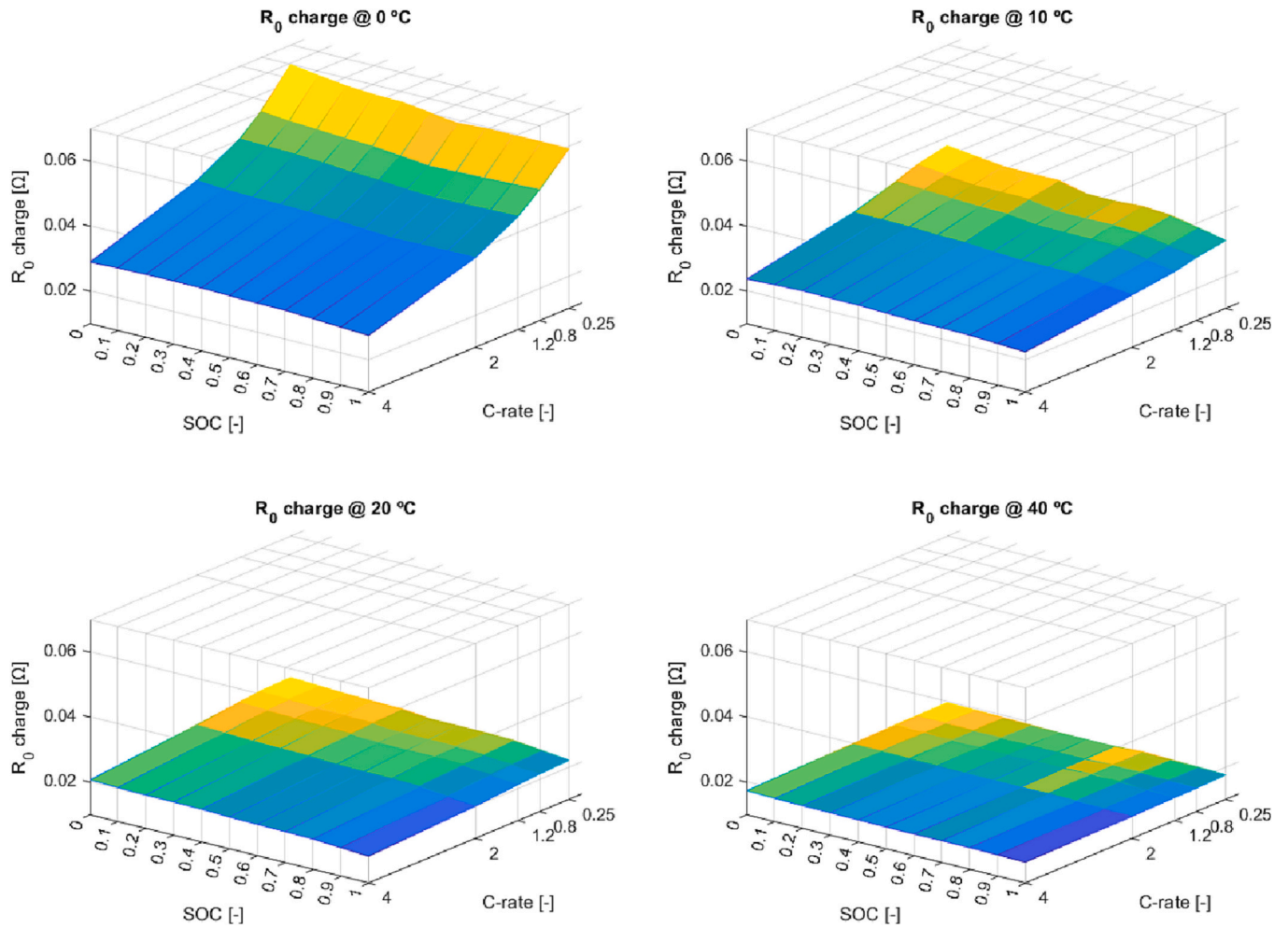**Fig. 5.** Ohmic resistance maps in discharge.

Fig. 6. Ohmic resistance maps in charge.

characterized by lower computational time and simple implementation. This aspect makes it suitable both for off-line studies, but also for the integration in control algorithms of a battery management system.

The electric model is a first order equivalent circuit model [31]: this means that the model can adequately represent the dynamic behavior of the battery, too, due to the double layer capacitance included in the equivalent circuit. In this model, represented in Fig. 1, four parameters need to be calibrated:

- The open circuit voltage (*OCV*) which represent the voltage delivered by the cell when it is in a balanced condition, that means when all the ohmic, activation and concentration polarization phenomena are terminated [32]. This parameter has been calibrated running quasi-static charges and discharges at C/40.
- The ohmic resistance (R_0) which represent the immediate voltage drop when applying a current due to ohmic losses inside the cell [33]. This parameter is affected by the temperature, the state of charge and the current. This parameter is determined running the hybrid power pulse characterization (HPPC) test at several temperatures [34].
- The charge transfer resistance (R_1) which represent the losses in the cell due to the migration of the ions from the solid phase (electrode) to the liquid phase (electrolyte). This parameter is determined running HPPC test at several temperatures.
- The double layer capacitance (C_1) which considers the dynamic behavior of the battery, and it is determined running HPPC test at several temperatures.

Apart from these parameters it is needed a characterization of the actual capacity of the cell. In fact, because in this model, a coulomb counting method is employed for the calculation of the state of charge of the cell (*SOC*), it is very important to have a precise estimation of the cell capacity in different temperature and discharge conditions: therefore, capacity tests have been run at different temperatures to get a map of this parameter [35].

The governing equations of this model are expressed by Eqs. (1) and (2):

$$v(t) = OCV(SOC(t)) - v_c(t) - R_0 I(t) \tag{1}$$

$$\frac{dv_c(t)}{dt} = \frac{1}{C_1}\left(I - \frac{v_c(t)}{R_1}\right) \tag{2}$$

On the other hand, the thermal behavior of the cell is represented with a nodal network [36]. This kind of model is based on an analogy with electrical circuit: the heat flows just like the current in an electrical circuit; as well the current goes from higher potential to lower potential, in the same way the heat flows from higher temperature to lower temperature. Each of the nodes of the model, represented in Fig. 2, are characterized in terms of dimensions (a volume is assigned), thermophysical properties (density, thermal conductivity, specific heat capacity). The nodes are connected between them by thermal resistances which can be conductive or convective ones, accordingly to the heat transfer process is considered [37]. In the model proposed in this work, the cell itself is represented with 4 solid nodes: one node is assigned to the core of the cell (node 2), two nodes are assigned to each of the
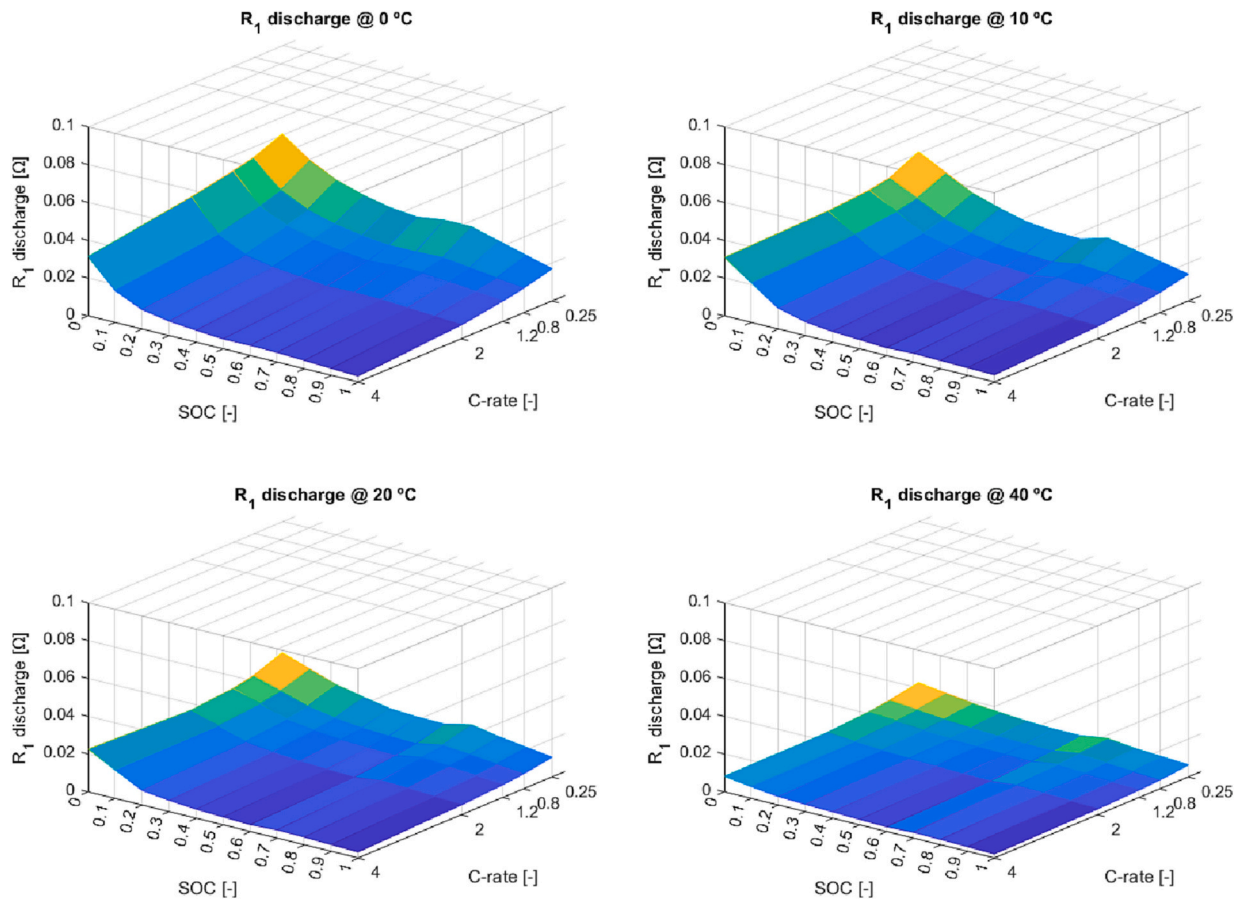
Fig. 7. Charge-transfer resistance maps in discharge.

terminals (nodes 1 and 3) and one node is assigned to the surface (node 4).

The governing equation of the thermal model, written for a generic node i is expressed by Eq. (3):

$$m_i c_i \frac{T_{t+\Delta t}^i - T_t^i}{\Delta t} = \sum_j K_{ij}\left(T_{t+\Delta t}^j - T_{t+\Delta t}^i\right) + \sum_k \dot{Q}_{k\to i} + \sum_j h_{ij} A_{ij}\left(T_f - T_{t+\Delta t}^i\right)$$

(3)

The term at the left hand of Eq. (3) represents the accumulated energy at the node i; the three terms at the right hand of Eq. (3) represent, respectively, the heat transferred conductively with the surrounding solid nodes, the heat generated in the node i, and the heat transferred convectively with surrounding fluid nodes (air or coolant).

The heat generation term in Eq. (3), in the case of a lithium-ion cell, corresponds to the irreversible heat generated by the cell during charge of discharge process [38], whose expression is reported in Eq. (4):

$$\dot{Q}_g = I \bullet (v - OCV)$$

(4)

The thermal parameters of the cell, such as the thermal capacity and the thermal conductivities in the axial and radial direction have been numerically determined fitting the experimental results and minimizing the error between the model and the measurement.

The cell's nodes are connected between them by conductive thermal resistances (R_{k1}, R_{k2}, R_{k3}). Then, if a stand-alone configuration is considered, the cell is only transferring heat with the surrounding air through the convective thermal resistance (R_{c2}). If, on the other hand, the cell is connected to other cells through a connection bar and it is cooled by a refrigerant flowing through a cold plate, some other nodes must be added to the nodal network for a complete representation of the system. The two terminals of the cell will be connected conductively to the electrical connection tabs through conductive thermal resistances (R_{k4} and R_{k5}). Furthermore, considering a serpentine cooling plate in contact with the lateral surface of the cylindrical lithium-ion cell, a conductive thermal resistance $R_{surf-foam}$ it will be considered for the heat transfer from the cell surface to the foam. The foam is necessary to guarantee a good thermal contact between the cell and the cold plate. Following this resistances' chain, the foam transfers heat conductively with the plate through the thermal resistance $R_{foam-plate}$, and finally the plate transfer heat convectively with the coolant flowing inside through the convective resistance $R_{plate-wg}$.

2.2. Experimental set-up

The lithium-ion cell considered for this analysis is a 32,700 cylindrical LFP cell, whose main characteristics are listed in Table 1.

This cell is tested with a battery tester from Arbin. The battery cycler is provided with 4 channels: each of this channel can provide 100 A and 10 V. The characteristics of the battery tester in terms of precision and resolution are provided in Table 2 [39].

The tests are run in a climatic chamber, which is needed to keep the ambient temperature constant during battery testing to precisely evaluate the cell performance at the desired temperature. The climatic chamber performance characteristics are listed in Table 3 [40].

The data are recorded with a data-logger system and the thermal measurement are made employing K-type thermocouples applied on the cell surface and terminals.
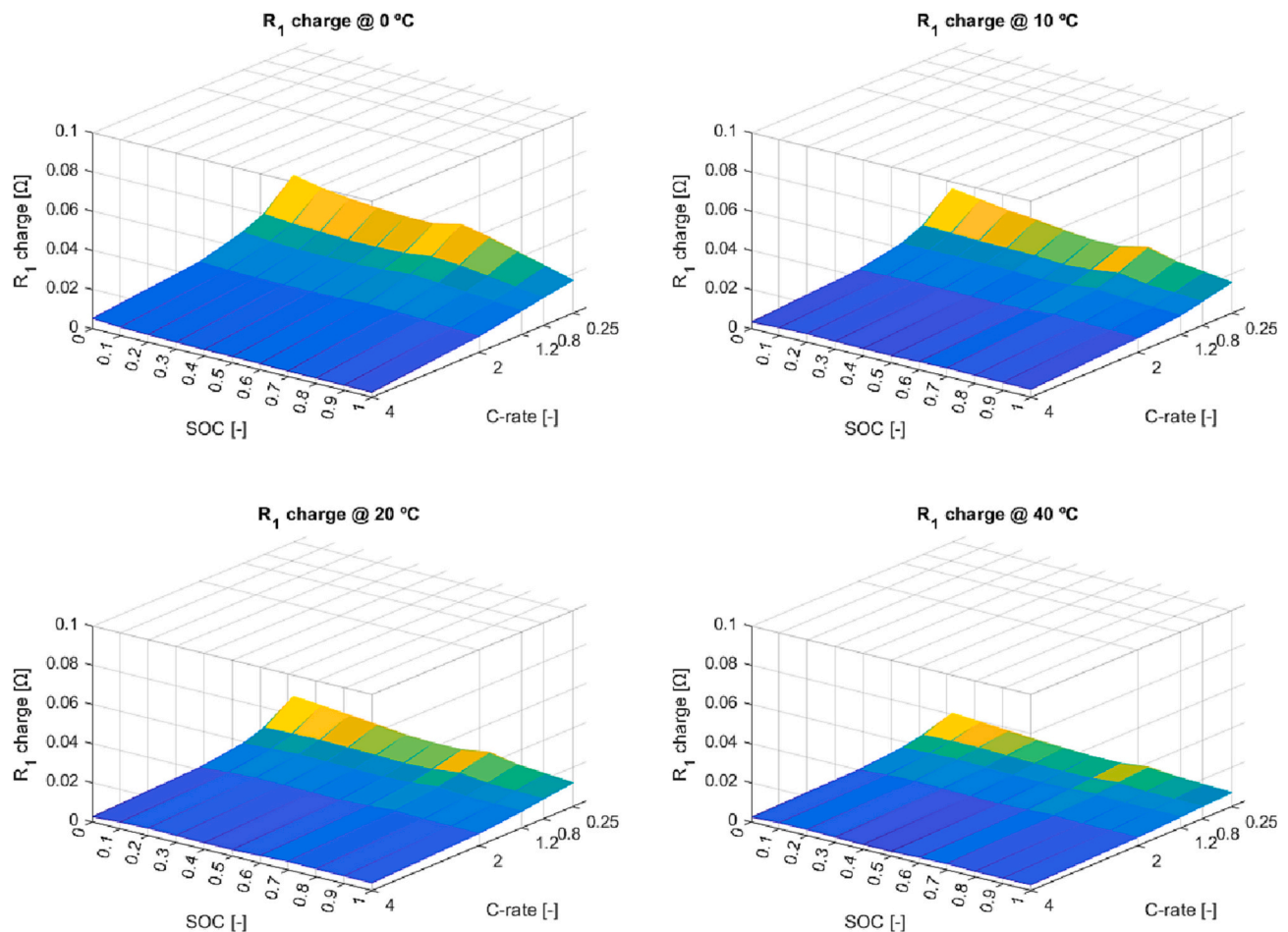
Fig. 8. Charge-transfer resistance maps in charge.

2.3. Characterization of cell parameters

The capacity test protocol considered for this analysis consists in a charge of the cell according to the CC-CV protocol, a rest of the cell of 1 h and a complete discharge of the cell [41]. The constant current is made always at 1C, and it finishes when the maximum voltage is achieved. The constant voltage phase consists in keeping the voltage equal to maximum voltage and letting the current go down until a cut-off condition is achieved: in this case the cut-off condition is achieved when the current is the 5 % of the charging current [41]. The results of the capacity test campaign are shown in Fig. 3, with respect to the temperature and the discharge rate. The capacity test has been run at 3 temperatures (0, 10 and 20 °C) and at 6 discharge rates (C/40, C/4, C/2, 1C, 2C and 4C).

From Fig. 3, it can be concluded that the capacity of the cell is greatly affected by the temperatures: in fact, as the temperature gets higher, also the cell capacity increases. This is because all the diffusion and charge transfer phenomena happening inside the cell are favored by higher temperatures. The behavior with respect to the c-rate is more difficult to interpret due to the overlapping of two phenomena: from one side, due to the Peukert effect [42], the cell capacity decreases at higher discharge rates; on the other hand, due to the self-heating effect and because at higher discharge rates, the heat generation is higher, the cell heats up and this surely favors an increase of the measured capacity [43]. The co-existence of these two opposite phenomena leads to a non-monotone behavior against the c-rate.

The open circuit voltage is estimated running quasistatic charges and discharges at C/40. This test is repeated at 3 different temperatures and the results are shown in Fig. 4 as a map with respect of the temperature

and the state of charge.

The open circuit voltage is very much affected by the state of charge: the higher is the state of charge of the cell, the higher is the open circuit voltage. Secondly, two maps are provided for the charge and the discharge, and this is because the lithium-ion cell is a system characterized by hysteresis. Finally, it must be noted that the temperature has not a great impact on the open circuit voltage: in fact, the dependency on temperature can be seen only when the cell is close to the fully discharged condition (for the discharge curves) and close to the fully charged condition (for the charge curve) [44].

Finally, the resistive and capacitive parameters of the lithium-ion cell have been determined by running HPPC tests at 0, 10, 20 and 40 °C. This test protocol has been widely considered in literature for determining lumped parameters of a lithium-ion cell. In this case, the protocol has been adapted to the pulse power capability of the lithium-ion cell [45]. Therefore, a series of pulses has been designed considering cell charge and discharge pulse current limits: pulses at C/4, 5C/6, 6C/5, 2C and 4C have been considered. It is important to consider different pulses because the resistive and capacitive parameters change according to charge/discharge rate considered. The test protocol consists of the following steps:

1. A full charge of the cell employing the CC-CV protocol.
2. A rest of 1 h.
3. A discharge of the 10 % of the cell capacity
4. A series of pulses, each of them 30 s long interspersed by 100-s-long rests.

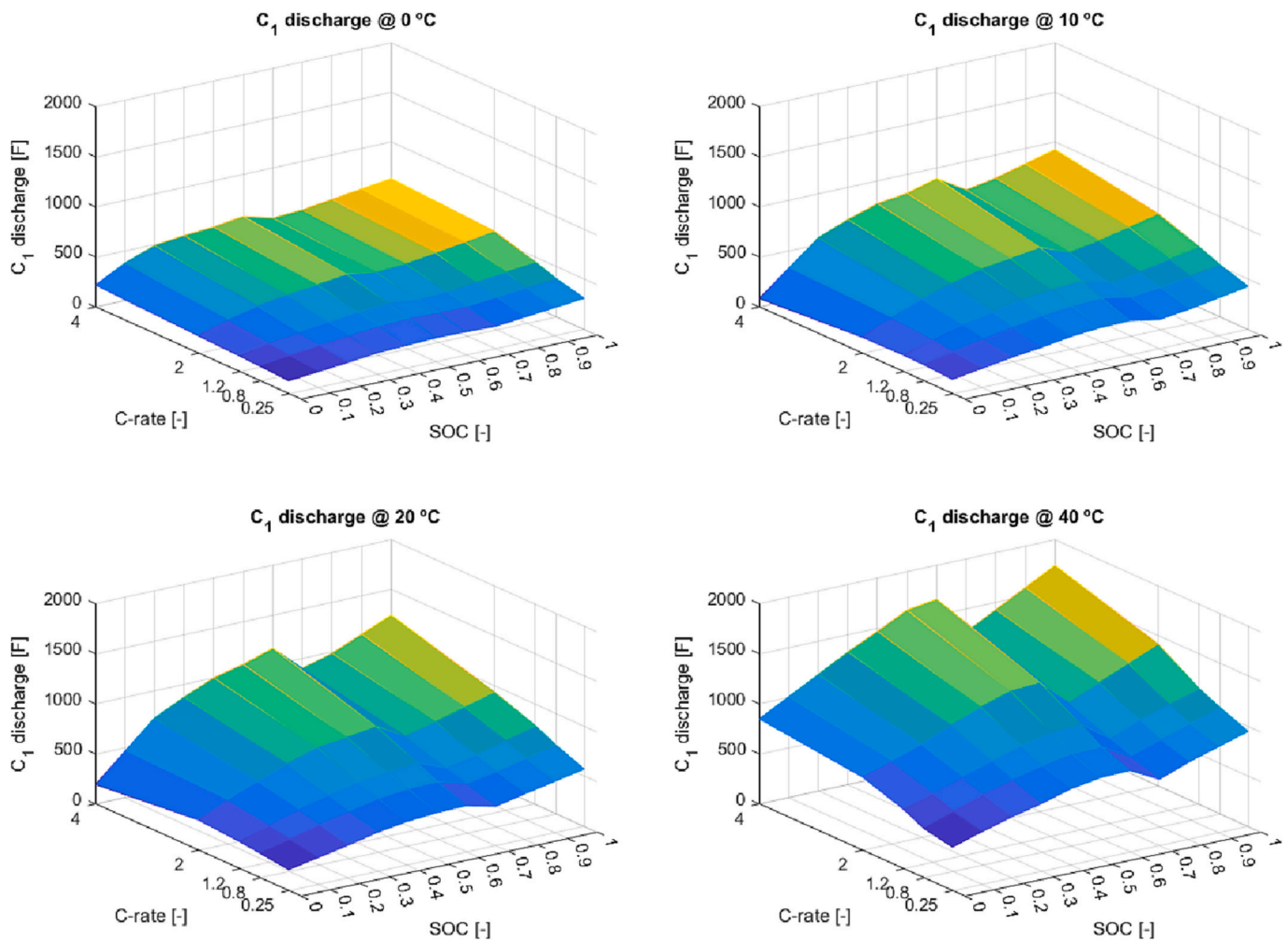The steps 3–4 are repeated 9 times: in this way, the pulses are

Fig. 9. Double layer capacitance maps in discharge.

repeated at 9 state of charge stages from 0.9 to 0.1. In this way, the dependency of resistive-capacitive parameters on state of charge is considered. The evaluation of the parameters at $SOC = [0, 1]$ is made by extrapolation of the results obtained experimentally at the evaluated state of charge stages. This decision is because a charge pulse at fully charged condition could lead the cell to an undesired overcharged condition; on the other hand, a discharge pulse at fully discharged condition could lead the cell to an undesired over discharge condition. To avoid these potentially negative conditions for the cell operability, the parameters in these extremal conditions have been extrapolated with appropriate physical extrapolation models.

The results of the calibration process for the parameters are shown from Figs. 5 to 10. The results are shown in terms of the maps with respect to the c-rate and SOC. For each parameter are provided maps at the four temperatures considered during the characterization campaign.

From Figs. 5 to 8, it can be understood that the resistive parameters decrease when the temperature gets higher: this is because all the diffusive phenomena are favored by higher temperatures, and this leads to lower resistance to the migration of lithium-ions from the electrodes to the electrolyte. Furthermore, it is observed that when the c-rate and the state of charge decrease, the resistances of the lithium-ions increase [46]. From Figs. 9 to 10, it is observed that when the temperature increases, the double layer capacitance increases. Finally, when the state of charge and the c-rate increase, the double layer capacitance increases.

2.4. Validation of the cell model

Once the cell parameters have been calibrated, the model has been validated using a dynamic power profile shown in Fig. 11. This cycle has been obtained from an initial RDE cycle of a hybrid vehicle: that is why it is characterized by this very dynamic behavior with instantaneous charge and discharge values.

The model has been validated at room temperature (23 °C) and for a stand-alone configuration. The model agreement with experimental results is provided in Fig. 12 both for the electrical model (voltage) and for thermal model (temperatures of the surface and the terminals). Since the error are kept all below the 1.5 %, the model is considered validated.

3. Model of the battery module

Once the cell model has been validated, it can be introduced a model of the battery module. The module analyzed is composed of 60 cells, with a configuration 12S5P, that means 12 cells in series and 5 cells in parallel. Given the specifications of the cell, it is possible to introduce the battery electrical specifications in Table 4.

The electro-thermal behavior of each cell is described according to the model validated in Section 2. Furthermore, the battery module cooling is obtained coupling the module with a serpentine cooling plate. The heat transfer from each cell to the cooling plate is considered with the thermal resistance from the cell to the coolant introduced in Fig. 2. A schematic view of the whole battery module is presented in Fig. 13.

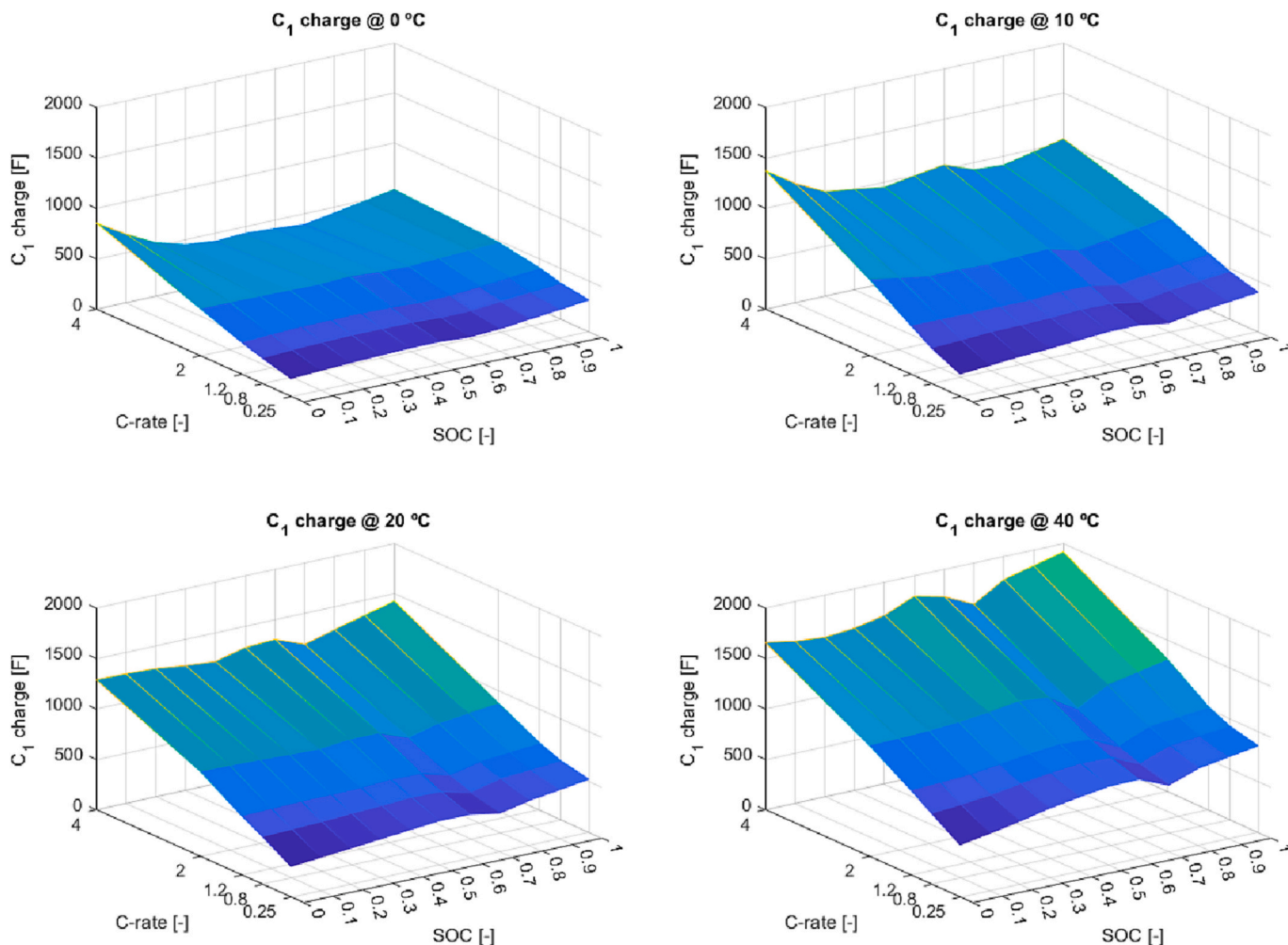The base working fluid is an ethylene glycol water solution (50 %

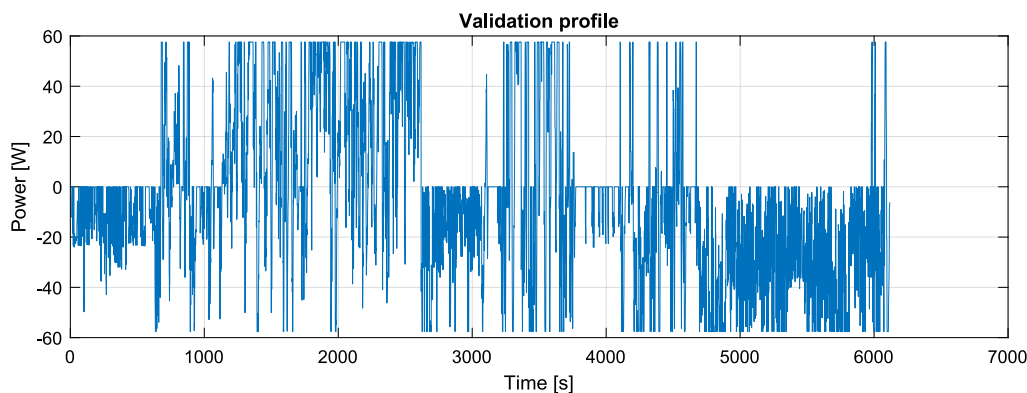**Fig. 10.** Double layer capacitance maps in charge.

Fig. 11. Power validation profile.

water – 50 % ethylene glycol). The thermal properties of this base fluid – density, thermal conductivity, dynamic viscosity, and specific heat capacity – are calculated with look up tables available in literature with respect to the fluid temperature.

Once calculated the base fluid thermo-physical properties, some other correlations must be introduced to consider the effect of the introduction of the nanoparticles in the fluid. These correlations are introduced in Subsection 3.1.

3.1. Thermo-physical properties of the nanofluid

In this section, the determination of density, thermal conductivity, viscosity, and specific heat capacity of the working fluid is provided. The following definitions are provided:

- *Nanoparticle*: it is considered to be a particle whose diameter ranges in between $1 - 100 \, nm$. These nanoparticles are typically metal
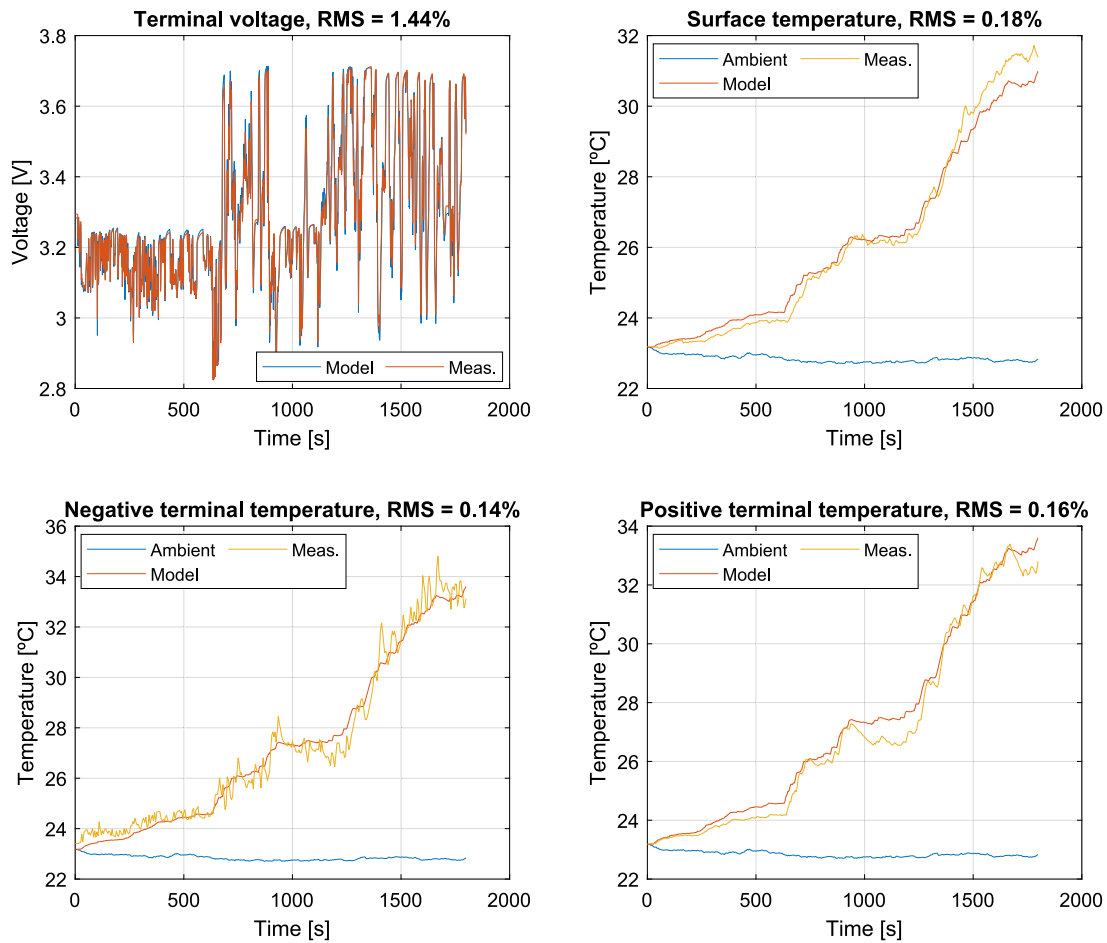
Fig. 12. Electro-thermal model validation.

Table 4
Battery module specifications.

Nominal capacity	30 Ah
Nominal voltage	38.4 V
Maximum voltage	43.8 V
Minimum voltage	24 V

oxides as well as metals or carbon nanotubes and they are added to the base fluid in order to improve its thermal properties.

- *Nano encapsulated phase-change material (NePCM)*: when the internal part of the nanoparticle, is constituted by a phase-change material, this core is defined NePCM, similarly to what have been considered in some other works [26,59].
- *Nanofluid*: in this work, nanofluid is the whole fluid composed by base fluid, nanoparticles and NePCMs, since a phase-change material component is considered always to be combined with a metal oxide nanoparticle.

The working fluid is defined such as the base fluid to which nanoparticles and NePCMs are added. The properties of the base fluid are indicated with the subscript *b*; the properties of the nanoparticle are indicated with the subscript *p*; the properties of the nanofluid (base fluid + nanoparticles + NePCMs) are indicated with the subscript *nf*.

In literature several works have proposed correlations for the estimation of thermo-physical properties of nanofluids.

The density of the working fluid is calculated according to the Eq. (5) of Pak and Cho [47,60], widely used in literature:

$$\rho_{nf} = \rho_p \bullet \varphi + \rho_b \bullet (1 - \varphi) \tag{5}$$

In this case the density is simply considered as a weighted average of the density of the nanofluid and the density of the base fluid. Considering that all the nanoparticles are characterized by a high value of density, the density of the nanofluid is higher than the base fluid one.

The thermal conductivity is the real key parameter for the nanofluids since the nanoparticles are characterized by very high values of thermal conductivity since they are metals [48]. In the literature, many models have been proposed to calculate the thermal conductivity of the nanofluid, and all these models find that the addition of nanofluids leads to a great increase of this parameter [49]. From a physical point of view, this increase of thermal conductivity has been explained in literature with the formation of nanolayers around the nanoparticles. The correlation of Yu and Choi [50,61] is used in this work to describe the effect of the addition of the nanoparticles to the base fluid as shown in the Eq. (6). The effect of the formation of the nanolayers is explained by the Maxwell correlation [51] as shown in Eq. (7).

$$k_{nf} = \frac{k_{pe} + 2k_b + 2\left(k_{pe} - k_b\right)(1 + \beta)^3 \varphi}{k_{pe} + 2k_b - \left(k_{pe} - k_b\right)(1 + \beta)^3 \varphi} k_b \tag{6}$$

$$k_{pe} = \frac{\left[2(1 - \gamma) + (1 + \beta)^3(1 + 2\gamma)\right]\gamma}{-(1 - \gamma) + (1 + \beta)^3(1 + 2\gamma)} k_p \tag{7}$$

The parameter β represents the ratio of nanolayer thickness to the nanoparticle radius while γ is the ratio of nanolayer thermal conductivity divided by nanoparticle thermal conductivity. The determination of the nanolayer thickness δ and the nanolayer thermal conductivity k_l is
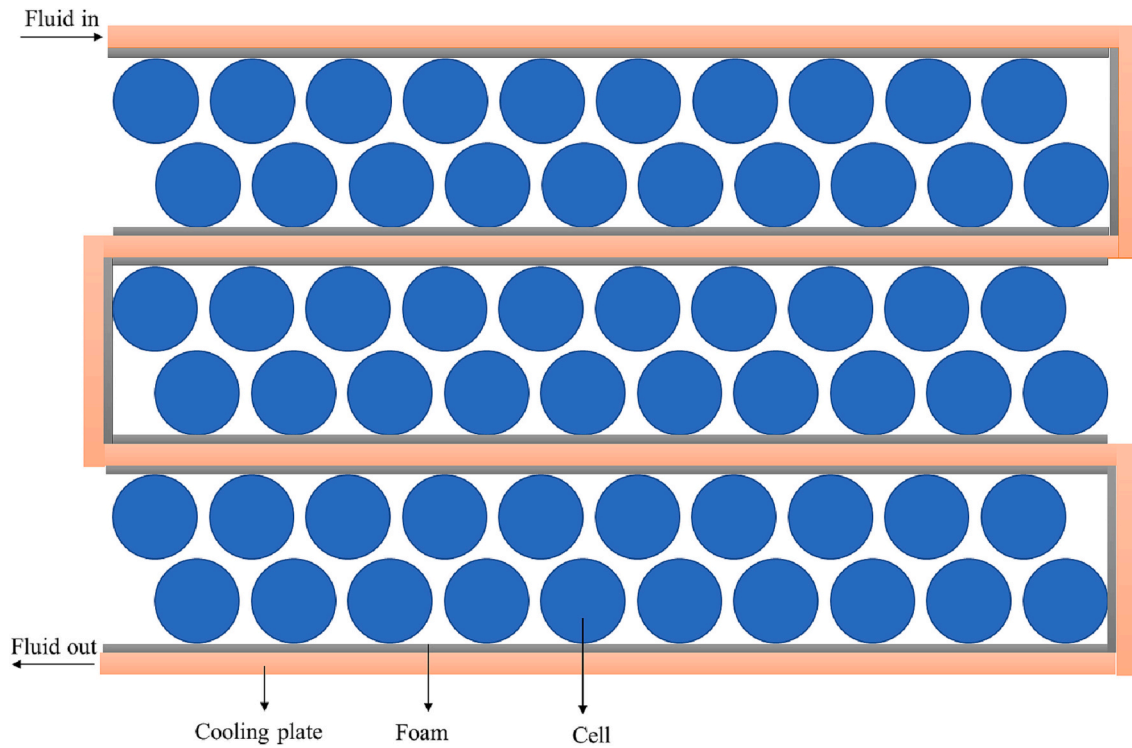
Fig. 13. Battery module geometry.

Table 5
Nanoparticles considered in this analysis.

Nanoparticle	Density [kg/m³]	Thermal conductivity [W/m • K]	Specific heat capacity [J/kg • K]
CuO	6500	32.9	551
Al2O3	3970	16.3	680
SiO2	2200	1.2	703
ZnO	5660	50	494
TiO2	4175	8.4	692

Table 6
NePCMs considered in this analysis.

	NePCM	Melting temperature [°C]	Heat of fusion [J/kg]
PCM1	5913-paraffin	23	189,000
PCM2	Hexadecane	18	236,000
PCM3	Heptadecane	22	213,000
PCM4	Octadecane	28	244,000
PCM5	Potassium fluoride hydrate	18.5	231,000
PCM6	Calcium chloride dihydrate	29.7	171,000

complicated and no experimental data are available [52]. Therefore, two simplifying hypotheses introduced by Maxwell are considered [26]:

- the ratio of nanolayer thickness divided by the nanoparticle radius is constant and it is equal to 0.1;
- the thermal conductivity of the nanolayer is equal to the thermal conductivity of the nanoparticle.

Maxwell observed that these simplifying hypotheses did not introduce a great error for low concentrations as the one considered in this work.

As well as for the thermal conductivity, also for the viscosity the literature provides with many available models [53]. The model which has been selected in this work is the model discussed by Wang [54] and it is based on a simplifying hypothesis: the model considers a suspension of s-hard spherical nanoparticles into the base fluid, and it does not consider the interaction among the nanoparticles. The model is expressed by the Eq. (8)

$$\mu_{nf} = \left(1 + 2.5\varphi + 6.2\varphi^2\right) \bullet \mu_b \tag{8}$$

Finally, the specific heat capacity needs to be calculated, too. In this work a nanofluid with nano encapsulated phase change materials is considered: therefore, calculating the specific heat capacity it is needed to take into account the contribution of the latent heat of the NePCM. Eq. (9) is introduced for the calculation of the specific heat capacity of the nanofluid as proposed by Torregrosa [26]:

$$c_{nf} = \frac{(1-\varphi)\rho_b c_b + \varphi\rho_p c_P}{(1-\varphi)\rho_b + \varphi\rho_p} + \frac{\varphi \bullet H_{NePCM}}{\Delta T} \bullet \pi \bullet sin\left(\frac{T_{fluid} - T_{fusion}}{\Delta T} \bullet \pi\right) \tag{9}$$

Therefore, in Eq. (9) two contributions are considered: a first one due to the addition of the nanoparticle to the base fluid and a second one due to the heat of fusion that is obtained during the change of phase of the NePCM core. The meaning of the second term of Eq. (9) is that only when the fluid temperature (T_{fluid}) is higher than the fusion temperature (T_{fusion}) this term is active, and there is an increase of the specific heat due to the heat of fusion of the NePCM. This contribution ends when the condition $sin\left(\frac{T_{fluid} - T_{fusion}}{\Delta T} \bullet \pi\right) = 0$ is verified and this happens when $T_{fluid} = T_{fusion} + \Delta T$.

3.2. Heat transfer coefficient estimation

Once all the thermo-physical properties of the fluid are calculated, it is possible to determine the Nusselt number. The Nusselt number is obtained using a correlation proposed by Dittus and Boelter [55] as shown in Eq. (10):
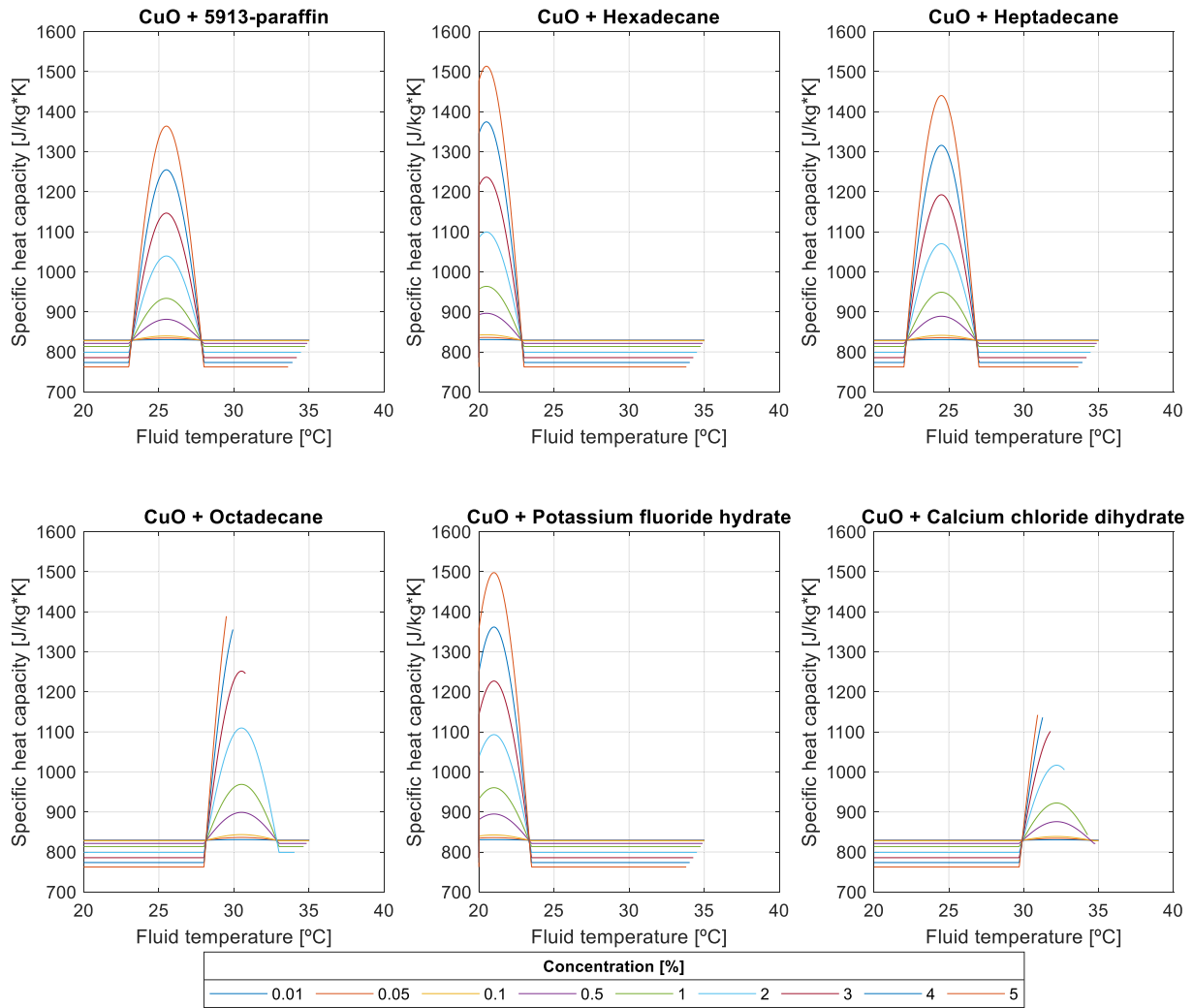
$$Nu = 0.023Re^{0.8}Pr^n \tag{10}$$

Fig. 14. Specific heat capacity versus fluid temperature for different CuO and NePCM concentrations.

This correlation has been calibrated for a developed flow in a pipeline and it is applied within the following hypotheses:

- $0.7 < Pr < 160$.
- $L/D > 40$.
- $n = 0.4$ when the temperature increases, $n = 0.3$ when the temperature decreases.

From the Nusselt number, finally, it is possible to get an estimation of the convective heat transfer coefficient h, according to the definition of Nusselt number:

$$h = \frac{Nu \bullet k}{L} \tag{11}$$

Finally, considering the expressions of the Reynolds and Prandtl number

$$Re = \frac{\rho u D}{\mu} \tag{12}$$

$$Pr = \frac{\mu c}{k}, \tag{13}$$

it is possible to mathematically quantify the positive effect of the addition of nanoparticles to the base fluid. In fact, considering Eqs. (12) and (13) it can be found that

$$\frac{Re_{nf}}{Re_b} = \left(\frac{\rho_{nf}}{\rho_b}\right)\left(\frac{u_{nf}}{u_b}\right)\left(\frac{\mu_{nf}}{\mu_b}\right)^{-1} \tag{14}$$

$$\frac{Pr_{nf}}{Pr_b} = \left(\frac{\mu_{nf}}{\mu_b}\right)\left(\frac{c_{nf}}{c_b}\right)\left(\frac{k_{nf}}{k_b}\right)^{-1} \tag{15}$$

From Eqs. (10), (11), (14) and (15), it can be finally found an expression for the effect of the nanoparticle addition with respect to the base fluid in terms of the convective heat transfer coefficient:

$$\frac{h_{nf}}{h_b} = \left(\frac{Re_{nf}}{Re_b}\right)^{0.8}\left(\frac{Pr_{nf}}{Pr_b}\right)^n\left(\frac{k_{nf}}{k_b}\right) \tag{16}$$

Eq. (16) gives a mathematical understanding of the increase and improvement of the heat transfer when adding nanoparticles to a basic fluid.

4. Analysis of different combinations of nanoparticles and NePCMs

In this section a numerical assessment of different combinations of nanoparticles and NePCMs is provided. The goal of this analysis is to analyze the thermal benefit that could be generated by employing nanofluid with respect to the base fluid.

The nanoparticles used for this analysis are listed in Table 5. The main characteristics of the nanoparticles (density, thermal conductivity,
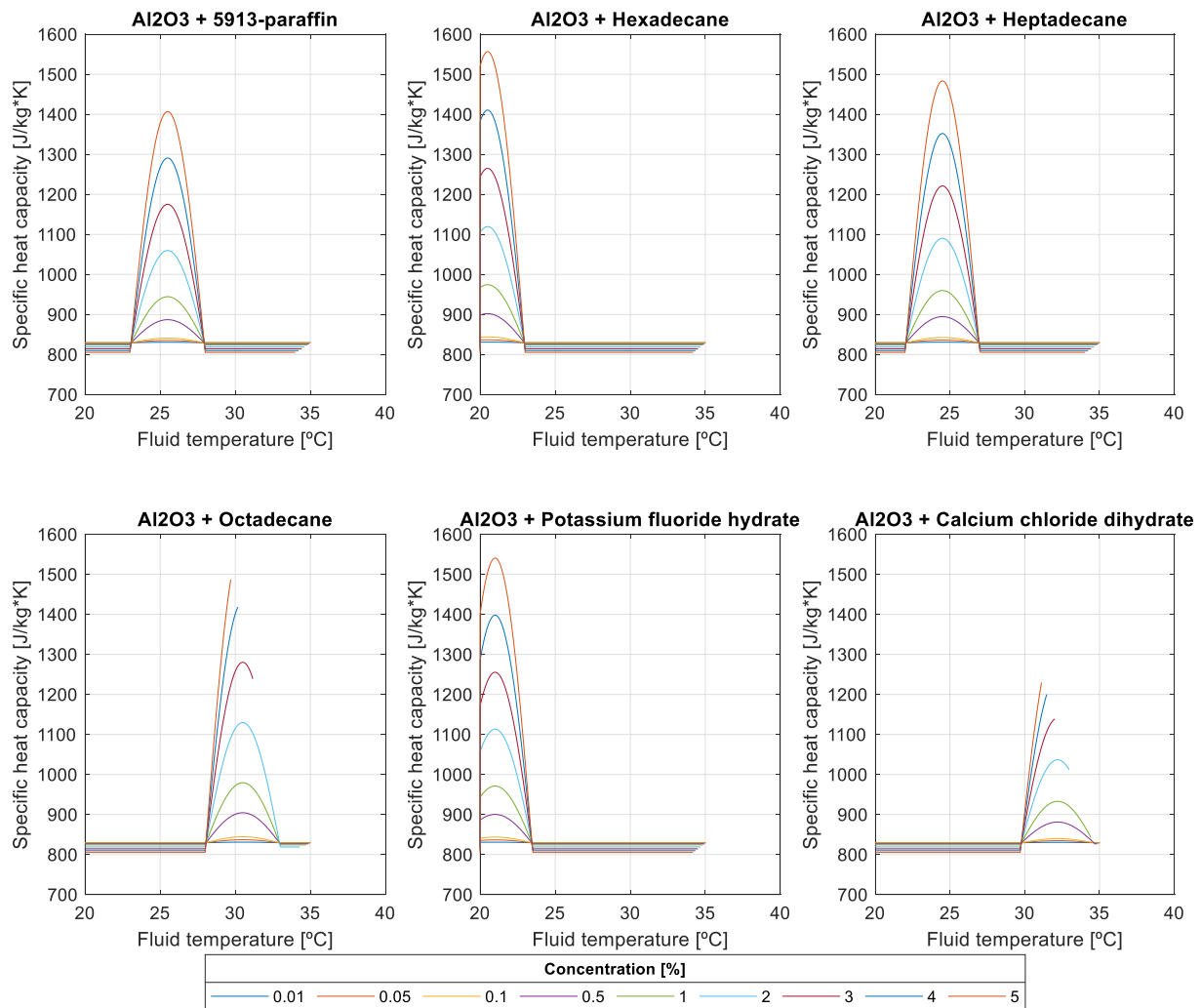
Fig. 15. Specific heat capacity versus fluid temperature for different Al2O3 and NePCM concentrations.

and specific heat capacity) are shown [56].

In this work a suspension of nanoparticle and NePCM is considered. Therefore, the NePCMs considered for this analysis are listed in Table 6 with their main characteristics [57].

The nanoparticles considered for this analysis have been chosen since they are widely used for lithium-ion battery cooling applications according to the most recent works available in literature. About the selection of the NePCMs, many review on use of nano encapsulated phase change materials for lithium-ion battery thermal management systems have been consulted such as the work of Malik et al. [57]. Among all the paraffins and inorganic PCMs reported in this work, the NePCMs with melting temperature in the optimal range of temperature of batteries have been considered (between 15 and 30 °C).

The comparison of the several nanofluids has been done for a fast-charging condition: a complete charging process from fully discharged condition $(SOC = 0)$ to fully charged condition $(SOC = 1)$ at 4C (charging process complete in around 900 s) has been considered. In this study, a volumetric flow of 2 l/min and ambient temperature of 20 °C have been chosen and the following conditions are analyzed:

- 9 different concentrations: [0.01 0.05 0.1 0.5 1 2 3 4 5]
- 5 different nanoparticles (Table 5)
- 6 different NePCMs (Table 6)

This wide parametric study (271 simulations) is aimed to identify the real benefit that is obtained by using a nanofluid, and which of the

analyzed nanofluids leads to the best performance in terms of maximum temperature reduction and maximum heat dissipated into the coolant.

First, in Figs. 14 to 18 the effect of the addition of the NePCMs on the specific heat capacity is shown. The shape of the curve is given by the fact that:

- when $T_{fluid} < T_{fusion}$, the melting process is not started yet: therefore, the specific heat capacity is constant, and it depends only on the concentration and the specific heat capacity of the nanoparticle;
- when $T_{fusion} < T_{fluid} < T_{fusion} + \Delta T$, the melting process of the NePCM core is happening: therefore. The increase of the specific heat capacity due to the heat of fusion of the NePCM is considered. The maximum of the specific heat capacity is achieved when $T_{fluid} = T_{fusion} + \frac{\Delta T}{2}$;
- when $T_{fluid} > T_{fusion} + \Delta T$, the melting process is already finished, and the specific heat capacity is constant from this temperature onwards.

The second aspect that can be appreciated in Figs. 14 to 18 is the impact of the concentration. Of course, the higher the volumetric fraction of nanofluid is, the more evident the effect on the specific heat capacity will be. It has been provided one figure for each nanoparticle considered in this analysis; then, for each nanoparticle, 6 plots are provided, one for each combination with NePCM. It is obvious that, the fluid temperature has a great impact on the positive effect of the NePCM introduction: in fact, the NePCM core will start to melt only when $T_{fluid} =$
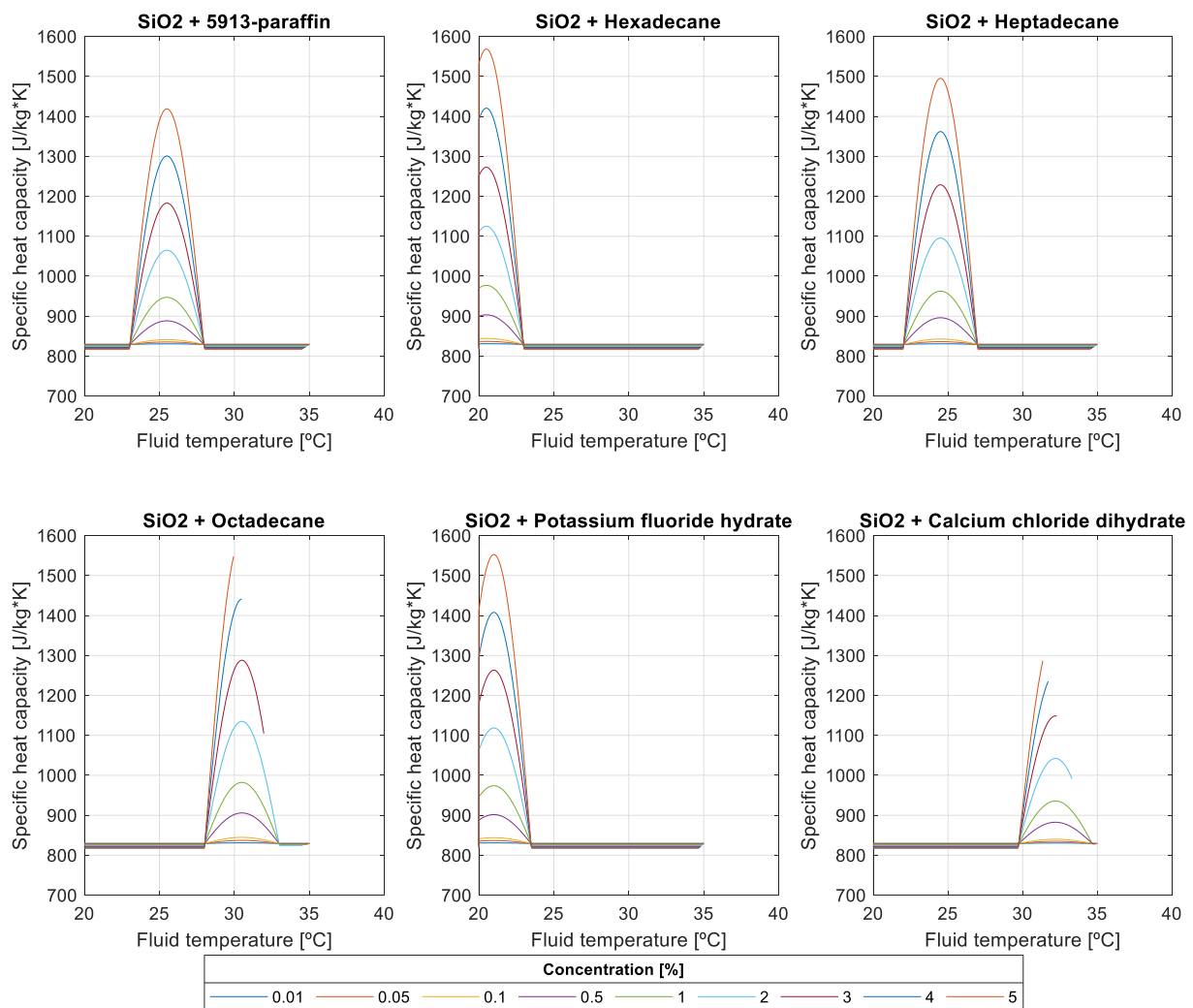
Fig. 16. Specific heat capacity versus fluid temperature for different SiO2 and NePCM concentrations.

T_{fusion} and just until $T_{fluid} = T_{fusion} + \Delta T$. For this reason, in the case of the hexadecane or potassium fluoride hydrate the sinusoidal part of the curve is just in the beginning of the charging process: the initial fluid temperature, in fact, is 20 °C, that is higher of the melting temperatures of these two NePCMs. On the other hand, if the octadecane of the calcium chloride dihydrate are considered, due to their higher melting temperature, the sinusoidal term of the specific heat is activated in the last part of the charging process. From these observations, the fluid temperature plays a very important role in this kind of thermal management system, and it should be taken into account in the NePCM's selection.

The nanofluid are compared in terms of maximum temperature reached in one of the cells of the module and the heat dissipated into the coolant during a 4C charging process. The boundary conditions are initial fluid temperature and ambient temperature equal to 20 °C and volumetric flow equal to 2 l/min.

The results in terms of maximum temperature in the cell are shown in Fig. 19.

The maximum temperature in the battery module is achieved at the end of the charging process. From Fig. 19, it is visible that the concentration is the parameter which most affects the thermal evolution of the battery module. When the concentration is lower than 1 %, a neglectable effect in this temperature is appreciated. For concentrations higher than 1 %, the decrease of the maximum temperature is increasingly higher. At 5 % of concentration, it is obtained a decrease of the temperature of

almost 2 °C. Another aspect which must be underlined is the importance of the NePCM that is combined with the nanoparticle: it is visible that the octadecane and the calcium chloride dihydrate lead to the greatest reduction compared to the other NePCMs. This is because, for the boundary conditions considered for this analysis, the melting process was favored by the higher melting temperature of these two NePCMs. The other NePCMs characterized by lower melting temperature don't lead to a great decrease of the maximum temperature in the battery module. This aspect highlights the importance of the boundary condition in this problem: if a lower range of fluid temperature had been chosen, the NePCMs with lower melting temperature would have been favored, because in their case, the melting process would have started before. This makes understand that the choice of the NePCM should be done considering the usual working temperature range of the fluid in the thermal management system, to maximize the positive effect of the melting process and take advantage of the heat of fusion released during the change of phase. The heat dissipated to the coolant is shown in Fig. 20.

The heat dissipated into the coolant, with the best nanofluid combination (CuO + Octadecane) is 126 kJ, that is 20 % higher than the heat dissipated without nanoparticles at all. This means that more heat is removed from the battery module, which is the main purpose of adding nanoparticles and NePCMs to the base fluid of the thermal management system.

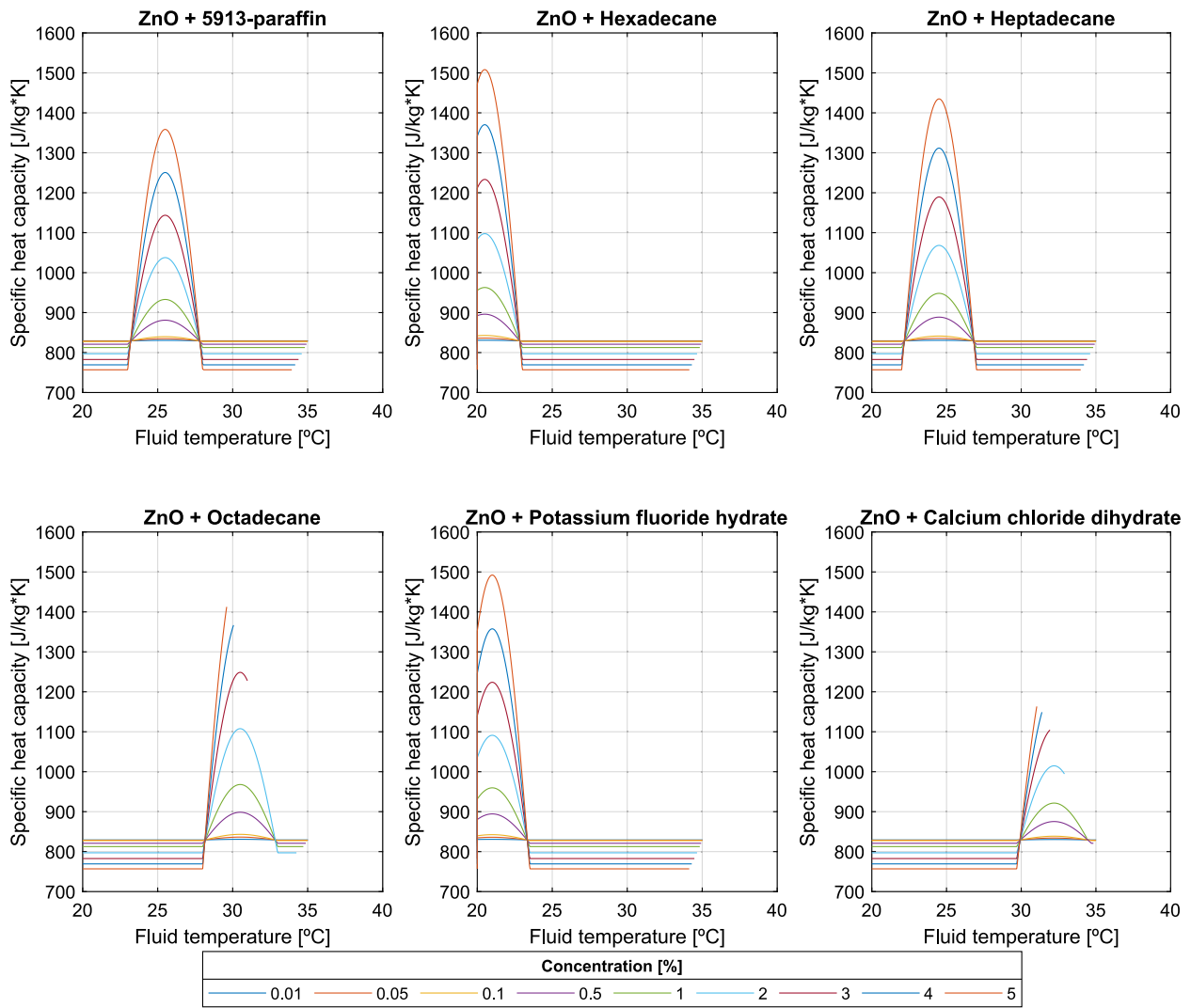The results so far analyzed show a great improvement of the nano-

Fig. 17. Specific heat capacity versus fluid temperature for different ZnO and NePCM concentrations.

fluid thermal performance with respect to the concentration: the higher the concentration is, the lower the maximum temperature in the battery module and the higher the heat dissipated into the coolant are. This could lead to the conclusion that as more nanoparticles are added to the system, the better is from a thermal point of view. Nonetheless, the volumetric fraction of nanoparticles in the system should be decided considering also the pressure drops in the system which cause more energy consumed by pump and auxiliars. In fact, considering the power consumed by the pump in Eq. (17) and the expression of the pressure drop in Eq. (18):

$$\dot{W}_b = \Delta P \bullet \dot{V} \tag{17}$$

$$\Delta P = f \frac{\rho u^2}{2D} L, \tag{18}$$

and considering a correlation for the estimation of the friction factor with respect to the Reynolds number:

$$f = f_{coef} \bullet Re^{-\frac{1}{4}}, \tag{19}$$

it is finally possible to conclude, considering Eqs. (5), (8), (14), (17), (18) and (19), that:

$$\frac{\dot{W}_{nf}}{\dot{W}_b} = \left(\varphi \bullet \left(\frac{\rho_p}{\rho_b} - 1 \right) + 1 \right)^{0.75} \left(1 + 2.5 \bullet \varphi + 6.2 \bullet \varphi^2 \right)^{0.25} \left(\frac{u_{nf}}{u_b} \right)^{2.75} \tag{20}$$

From Eq. (20) it is found a correlation between the power increase and the density and viscosity of the nanofluid. Since that density and viscosity of the nanofluid are functions of the volumetric fraction, the higher the volumetric fraction is, the higher the nanofluid density and viscosity are and this causes an increase of the power consumed by the pump [58].

From these considerations it can be concluded that the optimal volumetric fraction concentration should be found as a trade-off between the improvement of the thermal performance of the battery thermal management system and the containment of the pressure drops and the input power of the pump.

From this analysis, it has been found the importance of the choice of the NePCM to obtain a noticeable improvement from a thermal point of view. Therefore, in the next section, a design of experiment is proposed to understand which thermal properties of the NePCM affect the most the thermal performance of the nanofluid and how these parameters should be maximized or minimized.

5. Optimized nano encapsulated phase change material

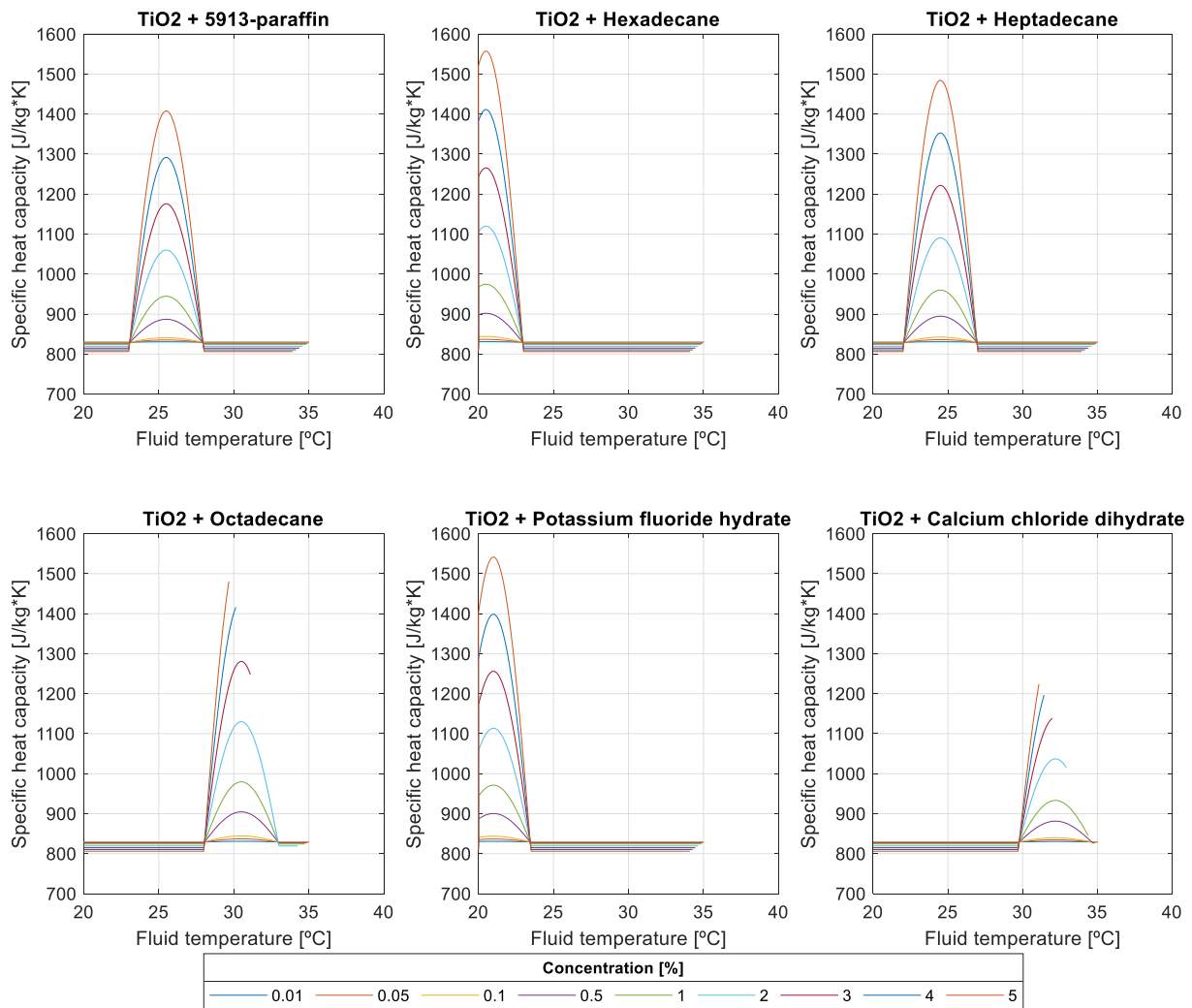In this section a design of experiment for the determination of the

Fig. 18. Specific heat capacity versus fluid temperature for different TiO2 and NePCM concentrations.

optimal characteristics of a NePCM is provided. In this case, the problem of pressure drop reduction is not considered, focusing the study only on the identification of the NePCM characteristics which mostly affect the cells temperature and the heat dissipation capability of the nanofluid.

To do that, the previously validated electro-thermal model (Section 2) is employed. As seen in Section 4, the thermal properties of a NePCM play a fundamental role in improving the performance of the thermal management system, and the NePCM should be chosen according to the usual working temperature of the fluid in order to take advantage of the heat of fusion release during the melting of the NePCM core. Therefore, for a given design point, it is proposed to find out optimized thermal properties of a NePCM and to find out which of these parameters affect mostly the thermal behavior of the battery module. The considered parameters are the concentration, the melting temperature, the characteristic temperature width and the heat of fusion. Therefore, the outcome of the design of experiment is to find out the dependencies of the three observed variables (maximum temperature, spatial temperature difference, heat dissipated into the coolant) with respect to the abovementioned parameters as follow in Eq. (21):

In this work, only single and double effects are considered, while triple and quadruple effects are neglected.

First of all, it is needed to define ranges for any of these thermal parameters, by defining lower and upper bounds. From the literature, it is justified to consider the ranges listed in Table 7.

Considering the 4 different parameters taken into account (φ, T_{fusion}, H_{NePCM}, ΔT), 17 different simulations have been run, considering the extreme point of the ranges of Table 7, plus a central point as it is listed in Table 8, since a full factorial design of experiment has been considered for this analysis.

A design point is chosen for this analysis considering a complete recharge of the battery module from fully discharged condition to fully charged condition at 4C. The charging process lasts about 900 s, and it is run with ambient temperature and initial fluid temperature equal to 20 °C and a volumetric flow of 2 l/min. From the design of experiment, the regression models are extracted for the maximum temperature, the spatial temperature difference and the heat dissipated:

$$\left[T_{MAX}, \Delta T_{cells}, H_{dissipated}\right] = f\left(\varphi, T_{fusion}, H_{NePCM}, \Delta T, \varphi \bullet T_{fusion}, \varphi \bullet H_{NePCM}, \varphi \bullet \Delta T, T_{fusion} \bullet H_{NePCM}, T_{fusion} \bullet \Delta T, H_{NePCM} \bullet \Delta T\right) \quad (21)$$
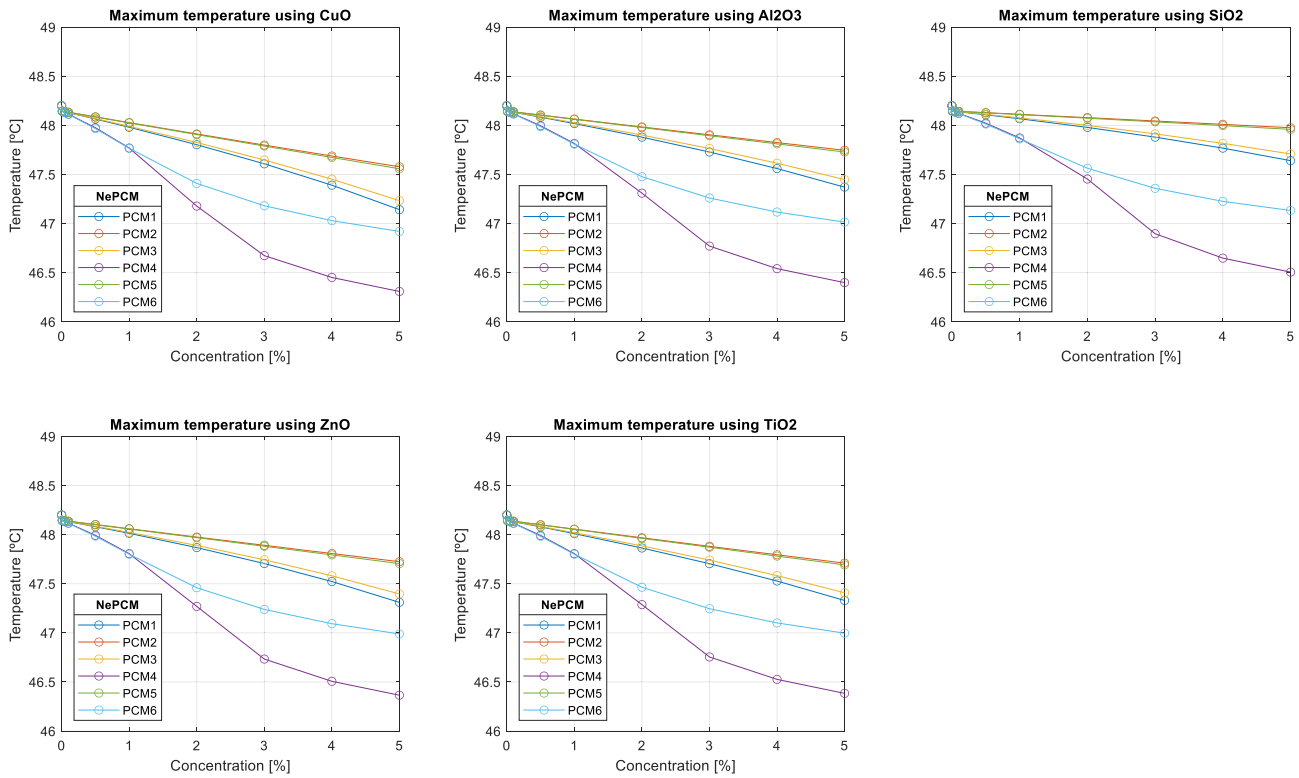
Fig. 19. Maximum temperature during 4C discharge process with combinations of different nanofluids and NePCMs.

$$
\begin{aligned}
\left[T_{MAX}, \Delta T_{cells}, H_{dissipated}\right] = {} & a_0 + a_{11} \bullet \varphi + a_{12} \bullet T_{fusion} + a_{13} \bullet H_{NePCM} + a_{14} \\
& \bullet \Delta T + a_{21} \bullet \varphi \bullet T_{fusion} + a_{22} \bullet \varphi \bullet H_{NePCM} + a_{23} \bullet \varphi \\
& \bullet \Delta T + a_{24} \bullet T_{fusion} \bullet H_{NePCM} + a_{25} \bullet T_{fusion} \\
& \bullet \Delta T + a_{26} \bullet H_{NePCM} \bullet \Delta T
\end{aligned}
\tag{22}
$$

The regression coefficients are listed in Table 9.

The regression model agreement with the simulation results is expressed in terms of coefficient of determination and for T_{MAX}, ΔT_{cells}, $H_{dissipated}$ they are respectively equal to $R^2_{T_{MAX}} = 93.3\%$, $R^2_{\Delta T_{cells}} = 92.5\%$, $R^2_{H_{dissipated}} = 85.5\%$.

Nonetheless, not all the effects initially considered, are statistically relevant. The Pareto chart, provided by the DoE analysis, shows all the effects from the most statistically relevant to the less statistically relevant. In the Pareto chart, a reference level is defined by a parameter α which indicates the significance level, and it is equal to 1 minus the confidence level for the analysis. The Pareto charts for the maximum temperature and the temperature spatial difference observed variables are shown in Fig. 21.

From the Pareto chart, both for T_{MAX} and for ΔT_{cells}, it can be concluded that the statistically relevant effects are the ones due to concentration, melting temperature and the combination of these 2 parameters. Furthermore, the dependent variable increases with respect of all the independent variables indicated by a clear row, and it decreases with respect of the ones indicated by a dark row.

For this reason, in Figs. 22 and 23 the results are shown as contour plots with respect of the melting temperature and the volumetric fraction within the ranges above specified. The results are shown for a specific characteristic temperature width of 5 °C and a heat of fusion of 200 kJ/kg.

Fig. 22 shows the dependencies of the maximum temperature and the spatial temperature difference with respect to the concentration and the melting temperature. It is visible that, given a melting temperature,

as the volumetric fraction gets higher, the maximum temperature and the spatial temperature difference decrease; at the same way, given a concentration, as the melting temperature of the NePCM is higher, the maximum temperature and the spatial temperature difference decrease. Furthermore, the dependency on volumetric fraction is by far the most important.

Fig. 23 shows the dependency of the total heat dissipated into the coolant with respect to the concentration and melting temperature. Oppositely from the other two variables, an increase in the volumetric flows and in the melting temperature leads to higher values of the heat dissipated and this is what is wanted to be achieved with the thermal management system.

It can be concluded that in the design point chosen for this analysis, melting temperature and volumetric fraction are the two parameters which mostly affect the benefit introduced by a NePCM. An increase of these two parameters generally leads to a better overall situation in terms of temperatures and heat dissipated.

6. Conclusions

This work proposes an assessment of use of nanoparticles and nano encapsulated phase change materials for a battery module cooling. A battery electro-thermal model is calibrated and validated experimentally. The numerical assessment and the design of experiment proposed in this study allow to conclude that:

- the only use of nanoparticles improves the fluid in terms of density and thermal conductivity characteristics, but to achieve meaningful improvement of the thermal management, the use of nano encapsulated phase change materials is needed to increase thermal heat capacity of the fluid;
- the numerical assessment has found that, for the given environment and working conditions analyzed, the octadecane and the calcium chloride dihydrate coupled with CuO are the two best combinations
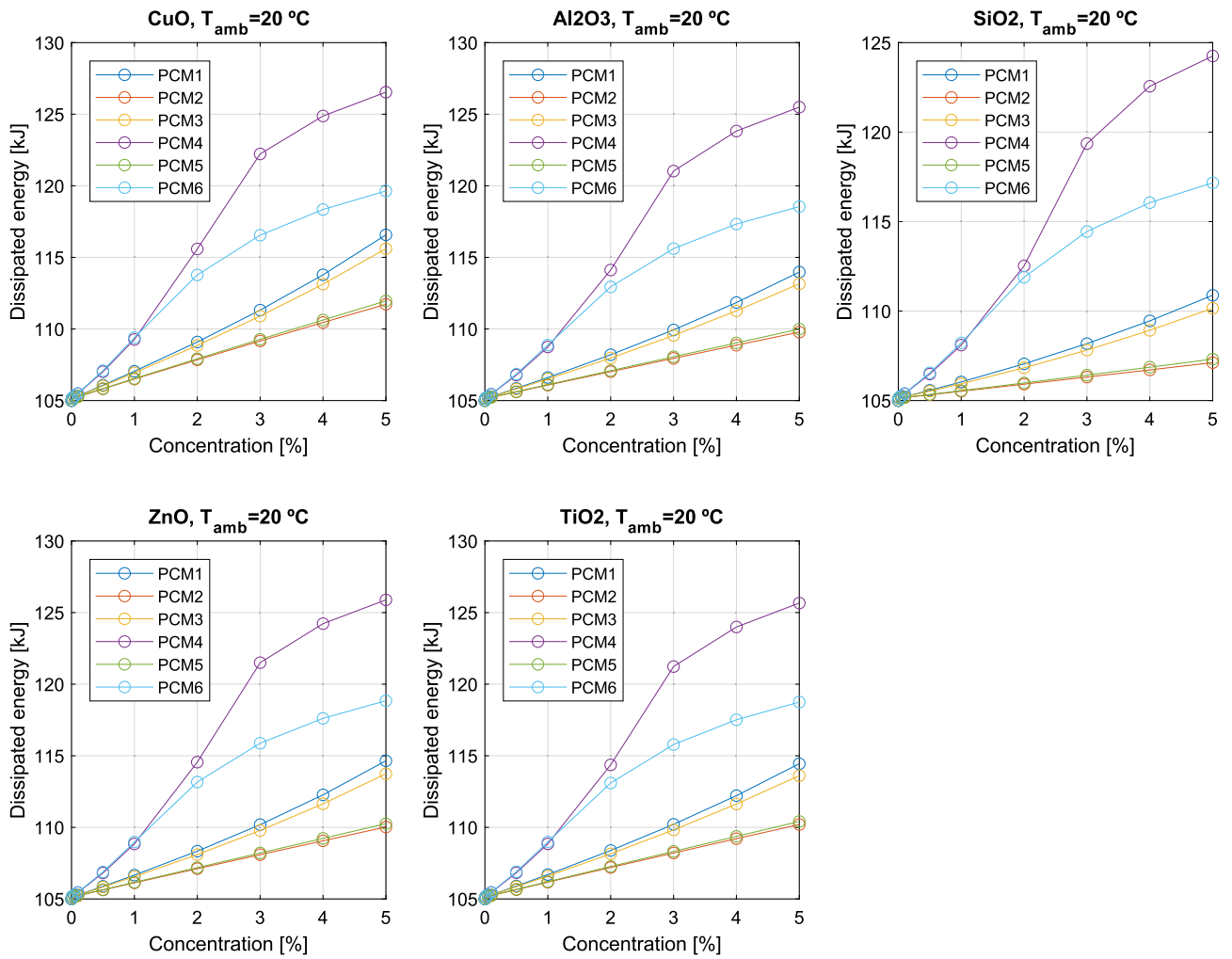
Fig. 20. Heat dissipated during 4C discharge process with different nanofluids and PCM.

Table 7
Ranges of thermal properties for design of experiment.

	Lower	Upper
Concentration [%]	0.1	5
Melting temperature [°C]	15	25
Characteristic temperature width [°C]	3	7
Heat of fusion [J/kg]	150,000	250,000

Table 8
Simulation run for the design of experiment.

Simulation	φ	T_{fusion}	H_{NePCM}	ΔT
1	0.1	15	150,000	3
2	0.1	15	150,000	7
3	0.1	15	250,000	3
4	0.1	15	250,000	7
5	0.1	25	150,000	3
6	0.1	25	150,000	7
7	0.1	25	250,000	3
8	0.1	25	250,000	7
9	5	15	150,000	3
10	5	15	150,000	7
11	5	15	250,000	3
12	5	15	250,000	7
13	5	25	150,000	3
14	5	25	150,000	7
15	5	25	250,000	3
16	5	25	250,000	7
17	2.55	20	200,000	5

Table 9
Regression coefficients.

Regression coefficient	T_{MAX}	ΔT_{cells}	$H_{dissipated}$
a_0	46.7	2.76	153.9
a_{11}	0.572	0.270	−5.75
a_{12}	0.109	0.0526	−2.44
a_{13}	−0.288	−0.139	−0.199
a_{14}	1.1E-05	5.2E-06	−2.3E-04
a_{21}	−0.0307	−0.014	0.013
a_{22}	0.0146	7E-02	0.0258
a_{23}	−1.4E0–6	−7E-07	2.4E-05
a_{24}	7E-03	3.4E-03	0.0142
a_{25}	-7.16E-07	−3.4E-07	1.2E-05
a_{26}	0.7.1E-07	3.5E-07	4-5E-07

to decrease maximum temperature in the battery module and avoid dangerous hazards;

- with the CuO + octadecane/calcium chloride dihydrate nanofluids, a 20 % increase of the heat dissipated into the coolant is found out, that means a significant improvement of the performance of the battery thermal management system;
- from the design of experiment is found that the volumetric fraction and the melting temperature are the two parameters with mostly affect the performance of the NePCM in the thermal management system;
- an increase of the concentration and of the melting temperature, for the design point given in this analysis, generally leads to a better
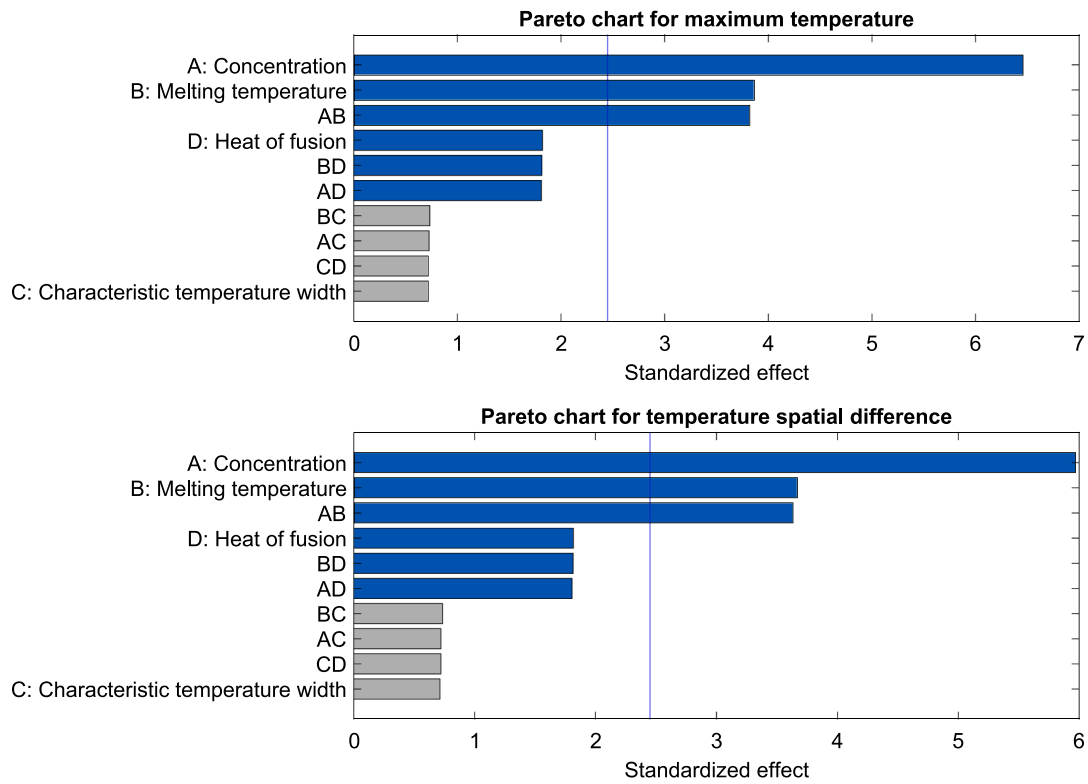
Pareto chart for maximum temperature

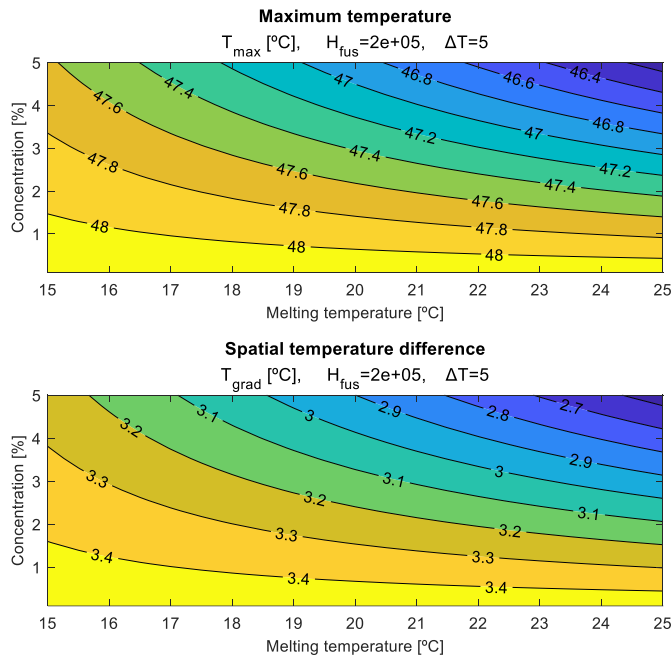**Pareto chart for temperature spatial difference**

Fig. 21. Pareto chart for maximum temperature and temperature spatial difference.

Maximum temperature

Spatial temperature difference

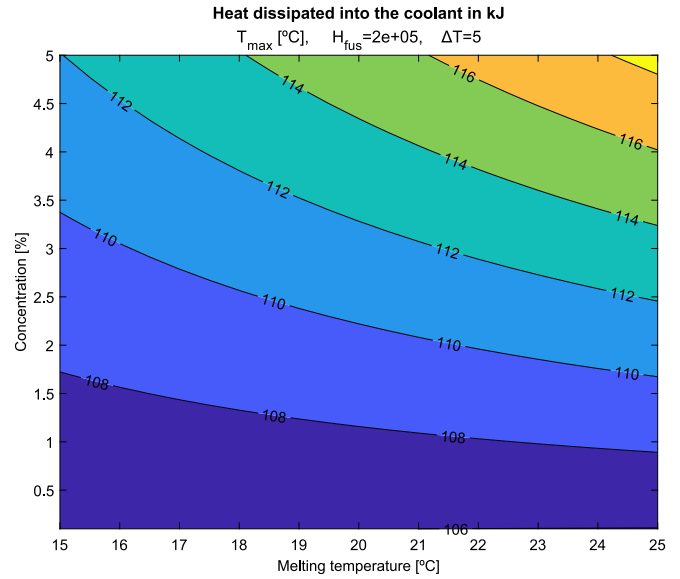**Fig. 22.** Contour plots for maximum temperature and spatial temperature difference.

overall situation (lower temperatures and higher heat dissipated into the coolant);

- the volumetric fraction in a real system should be found as a trade-off between the need to improve the cooling capability of the thermal management system and the need to avoid an excessive increase of the pressure drops in the system.

Heat dissipated into the coolant in kJ

Fig. 23. Contour plot for total heat dissipated into the coolant.

CRediT authorship contribution statement

Antonio José Torregrosa: Conceptualization, Methodology. **Alberto Broatch** Formal Analysis, Investigation, Methodology. **Pablo Olmeda**: Formal Analysis, Supervision, Writing- Reviewing and Editing. **Luca Agizza**: Investigation, Software, Validation, Data curation, Writing- Original draft preparation.

Declaration of competing interest

The authors declare that they have no known competing financial interests or personal relationships that could have appeared to influence the work reported in this paper.

Data availability

The data that has been used is confidential.

Acknowledgments

References

[1] A. Razmjoo, A. Ghazanfari, M. Jahangiri, E. Franklin, M. Denai, M. Marzband, A. Maheri, A comprehensive study on the expansion of electric vehicles in Europe, Appl. Sci. 12 (22) (2022) 11656.

[2] A. Garcia, J. Monsalve-Serrano, D. Villalta, S. Tripathi, Electric Vehicles vs e-Fuelled ICE Vehicles: Comparison of Potentials for Life Cycle CO 2 Emission Reduction (No. 2022-01-0745). SAE Technical Paper, 2022.

[3] M. Muratori, M. Alexander, D. Arent, M. Bazilian, P. Cazzola, E.M. Dede, J. Ward, The rise of electric vehicles—2020 status and future expectations, Prog. Energy 3 (2) (2021), 022002.

[4] T.M. Bandhauer, S. Garimella, T.F. Fuller, A critical review of thermal issues in lithium-ion batteries, J. Electrochem. Soc. 158 (3) (2011) R1.

[5] S. Ma, M. Jiang, P. Tao, C. Song, J. Wu, J. Wang, W. Shang, Temperature effect and thermal impact in lithium-ion batteries: a review, Prog. Nat. Sci.: Mater. Int. 28 (6) (2018) 653–666.

[6] L. Zhao, M. Zheng, J. Zhang, H. Liu, W. Li, M. Chen, Numerical modeling of thermal runaway for low temperature cycling lithium-ion batteries, J. Energy Storage 63 (2023), 107053.

[7] H. Yan, K.C. Marr, O.A. Ezekoye, Thermal runaway behavior of nickel–manganese–cobalt 18650 lithium-ion cells induced by internal and external heating failures, J. Energy Storage 45 (2022), 103640.

[8] C. Yang, H. Xi, M. Wang, Structure optimization of air cooling battery thermal management system based on lithium-ion battery, J. Energy Storage 59 (2023), 106538.

[9] I. Mokashi, A. Afzal, S.A. Khan, N.A. Abdullah, M.H.B. Azami, R.D. Jilte, O.D. Samuel, Nusselt number analysis from a battery pack cooled by different fluids and multiple back-propagation modelling using feed-forward networks, Int. J. Therm. Sci. 161 (2021), 106738.

[10] G. Xia, L. Cao, G. Bi, A review on battery thermal management in electric vehicle application, J. Power Sources 367 (2017) 90–105.

[11] D. Koster, A. Marongiu, D. Chahardahcherik, C.F. Braun, D. Schulte, E. Figgemeier, Degradation analysis of 18650 cylindrical cell battery pack with immersion liquid cooling system. Part 1: aging assessment at pack level, J. Energy Storage 62 (2023), 106839.

[12] M. Bernagozzi, A. Georgoulas, N. Miche, M. Marengo, Heat pipes in battery thermal management systems for electric vehicles: a critical review, Appl. Therm. Eng. 119495 (2022).

[13] A.G. Olabi, H.M. Maghrabie, O.H.K. Adhari, E.T. Sayed, B.A. Yousef, T. Salamah, M.A. Abdelkareem, Battery thermal management systems: recent progress and challenges, Int. J. Thermofluids 100171 (2022).

[14] N. Gallandat, J. Bérard, F. Abbet, A. Züttel, Small-scale demonstration of the conversion of renewable energy to synthetic hydrocarbons, Sustain. Energy Fuels 1 (8) (2017) 1748–1758.

[15] Z. Rao, Y. Huo, X. Liu, G. Zhang, Experimental investigation of battery thermal management system for electric vehicle based on paraffin/copper foam, J. Energy Inst. 88 (3) (2015) 241–246.

[16] G. Karimi, X. Li, Thermal management of lithium-ion batteries for electric vehicles, Int. J. Energy Res. 37 (1) (2013) 13–24.

[17] X. Li, Z. Zhou, M. Zhang, F. Zhang, X. Zhou, A liquid cooling technology based on fluorocarbons for lithium-ion battery thermal safety, J. Loss Prev. Process Ind. 78 (2022), 104818.

[18] X.H. Yang, S.C. Tan, J. Liu, Thermal management of Li-ion battery with liquid metal, Energy Convers. Manag. 117 (2016) 577–585.

[19] A. Can, F. Selimefendigil, H.F. Öztop, A review on soft computing and nanofluid applications for battery thermal management, J. Energy Storage 53 (2022), 105214.

[20] N. Sezer, M.A. Atieh, M. Koç, A comprehensive review on synthesis, stability, thermophysical properties, and characterization of nanofluids, Powder Technol. 344 (2019) 404–431.

[21] A.M. Sefidan, A. Sojoudi, S.C. Saha, Nanofluid-based cooling of cylindrical lithium-ion battery packs employing forced air flow, Int. J. Therm. Sci. 117 (2017) 44–58.

[22] M. Tousi, A. Sarchami, M. Kiani, M. Najafi, E. Houshfar, Numerical study of novel liquid-cooled thermal management system for cylindrical Li-ion battery packs under high discharge rate based on AgO nanofluid and copper sheath, J. Energy Storage 41 (2021), 102910.

[23] B. Mondal, C.F. Lopez, P.P. Mukherjee, Exploring the efficacy of nanofluids for lithium-ion battery thermal management, Int. J. Heat Mass Transf. 112 (2017) 779–794.

[24] A. Sarchami, M. Tousi, M. Kiani, A. Arshadi, M. Najafi, M. Darab, E. Houshfar, A novel nanofluid cooling system for modular lithium-ion battery thermal management based on wavy/stair channels, Int. J. Therm. Sci. 182 (2022), 107823.

[25] F. Jamil, H.M. Ali, M.A. Nasir, M. Karahan, M.M. Janjua, A. Naseer, R.A. Pasha, Evaluation of photovoltaic panels using different nano phase change material and a concise comparison: an experimental study, Renew. Energy 169 (2021) 1265–1279.

[26] A.J. Torregrosa, A. Broatch, P. Olmeda, A. Dreif, Assessment of the improvement of internal combustion engines cooling system using nanofluids and nanoencapsulated phase change materials, Int. J. Engine Res. 22 (6) (2021) 1939–1957.

[27] Y. Cao, I.B. Mansir, A. Mouldi, F. Aouaini, S.M. Bouzgarrou, R. Marzouki, A. Mohamed, Designing a system for battery thermal management: cooling LIBs by nano-encapsulated phase change material, Case Stud. Therm. Eng. 33 (2022), 101943.

[28] A. Qaderi, F. Veysi, Investigation of a water-NEPCM cooling thermal management system for cylindrical 18650 Li-ion batteries, Energy 244 (2022), 122570.

[29] J. Gu, J. Du, Y. Li, J. Li, L. Chen, Y. Chai, Y. Li, Preparation and characterization of n-Octadecane@ SiO2/GO and n-Octadecane@ SiO2/Ag nanoencapsulated phase change material for immersion cooling of Li-ion battery, Energies 16 (3) (2023) 1498.

[30] Q. Huang, X. Li, G. Zhang, J. Deng, C. Wang, Thermal management of Lithium-ion battery pack through the application of flexible form-stable composite phase change materials, Appl. Therm. Eng. 183 (2021), 116151.

[31] B.Y. Liaw, G. Nagasubramanian, R.G. Jungst, D.H. Doughty, Modeling of lithium ion cells—a simple equivalent-circuit model approach, Solid State Ionics 175 (1–4) (2004) 835–839.

[32] Q.Q. Yu, R. Xiong, L.Y. Wang, C. Lin, A comparative study on open circuit voltage models for lithium-ion batteries, Chin. J. Mech. Eng. 31 (1) (2018) 1–8.

[33] A. Rahmoun, H. Biechl, Modelling of Li-ion batteries using equivalent circuit diagrams, Prz. Elektrotech. 88 (7) (2012) 152–156.

[34] A. Nikolian, Y. Firouz, R. Gopalakrishnan, J.M. Timmermans, N. Omar, P. Van den Bossche, J. Van Mierlo, Lithium ion batteries—development of advanced electrical equivalent circuit models for nickel manganese cobalt lithium-ion, Energies 9 (5) (2016) 360.

[35] K.S. Ng, C.S. Moo, Y.P. Chen, Y.C. Hsieh, Enhanced coulomb counting method for estimating state-of-charge and state-of-health of lithium-ion batteries, Appl. Energy 86 (9) (2009) 1506–1511.

[36] A. Broatch, P. Olmeda, X. Margot, L. Agizza, A generalized methodology for lithium-ion cells characterization and lumped electro-thermal modelling, Appl. Therm. Eng. 217 (2022), 119174.

[37] M. Akbarzadeh, T. Kalogiannis, J. Jaguemont, J. He, L. Jin, M. Berecibar, J. Van Mierlo, Thermal modeling of a high-energy prismatic lithium-ion battery cell and module based on a new thermal characterization methodology, J. Energy Storage 32 (2020), 101707.

[38] S. Du, M. Jia, Y. Cheng, Y. Tang, H. Zhang, L. Ai, Y. Lai, Study on the thermal behaviors of power lithium iron phosphate (LFP) aluminum-laminated battery with different tab configurations, Int. J. Therm. Sci. 89 (2015) 327–336.

[39] ARBIN, "ARBIN INSTRUMENTS Laboratory Battery Testing System For Cell Applications Product Description Experts in Test Instrumentation," vol. 1, no. 979, pp. 1–7. https://www.arbin.com/products/battery-test-equipment/cell-testing/ (accessed 28 February 2023).

[40] ESPEC, ESPEC Environmental Test Chambers, Temperature (& Humidity) Chambers. https://www.espec.co.jp/english/products/env-test/. (Accessed 28 February 2023).

[41] M.A. Monem, K. Trad, N. Omar, O. Hegazy, B. Mantels, G. Mulder, J. Van Mierlo, Lithium-ion batteries: evaluation study of different charging methodologies based on aging process, Appl. Energy 152 (2015) 143–155.

[42] R. O'Malley, L. Liu, C. Depcik, Comparative study of various cathodes for lithium ion batteries using an enhanced Peukert capacity model, J. Power Sources 396 (2018) 621–631.

[43] Z.G. Qu, Z.Y. Jiang, Q. Wang, Experimental study on pulse self–heating of lithium–ion battery at low temperature, Int. J. Heat Mass Transf. 135 (2019) 696–705.

[44] D. Wycisk, G.K. Mertin, M. Oldenburger, A. Latz, Analysis of heat generation due to open-circuit voltage hysteresis in lithium-ion cells, J. Energy Storage 61 (2023), 106817.

[45] S. Liu, J. Chen, C. Zhang, L. Jin, Q. Yang, Experimental study on lithium-ion cell characteristics at different discharge rates, J. Energy Storage 45 (2022), 103418.

[46] Y. Xie, X. Wang, W. Li, Y. Zhang, D. Dan, K. Li, P. Wang, A resistance-based electro-thermal coupled model for an air-cooled battery pack that considers branch current variation, Int. J. Therm. Sci. 159 (2021), 106611.

[47] W. Duangthongsuk, S. Wongwises, Effect of thermophysical properties models on the predicting of the convective heat transfer coefficient for low concentration nanofluid, Int. Commun. Heat Mass Transf. 35 (10) (2008) 1320–1326.

[48] M.H. Esfe, M.K. Amiri, A. Alirezaie, Thermal conductivity of a hybrid nanofluid, J. Therm. Anal. Calorim. 134 (2) (2018) 1113–1122.

[49] H.Ş. Aybar, M. Sharifpur, M.R. Azizian, M. Mehrabi, J.P. Meyer, A review of thermal conductivity models for nanofluids, Heat Transf. Eng. 36 (13) (2015) 1085–1110.

[50] W. Yu, S.U.S. Choi, The role of interfacial layers in the enhanced thermal conductivity of nanofluids: a renovated Hamilton–Crosser model, J. Nanopart. Res. 6 (2004) 355–361.

[51] C.Y. Tso, S.C. Fu, C.Y. Chao, A semi-analytical model for the thermal conductivity of nanofluids and determination of the nanolayer thickness, Int. J. Heat Mass Transf. 70 (2014) 202–214.

[52] E.C. Okonkwo, I. Wole-Osho, I.W. Almanassra, Y.M. Abdullatif, T. Al-Ansari, An updated review of nanofluids in various heat transfer devices, J. Therm. Anal. Calorim. 145 (2021) 2817–2872.

[53] A. Hemmati-Sarapardeh, A. Varamesh, M.M. Husein, K. Karan, On the evaluation of the viscosity of nanofluid systems: modeling and data assessment, Renew. Sust. Energ. Rev. 81 (2018) 313–329.

[54] L. Wang, Y. Wang, X. Yan, X. Wang, B. Feng, Investigation on viscosity of Fe3O4 nanofluid under magnetic field, Int. Commun. Heat Mass Transf. 72 (2016) 23–28.

[55] D. Taler, J. Taler, Simple heat transfer correlations for turbulent tube flow, in: E3S Web of Conferences vol. 13, EDP Sciences, 2017, p. 02008.

[56] G. Liao, W. Wang, F. Zhang, E. Jiaqiang, J. Chen, E. Leng, Thermal performance of lithium-ion battery thermal management system based on nanofluid, Appl. Therm. Eng. 216 (2022), 118997.

[57] M. Malik, I. Dincer, M.A. Rosen, Review on use of phase change materials in battery thermal management for electric and hybrid electric vehicles, Int. J. Energy Res. 40 (8) (2016) 1011–1031.

[58] M. Awais, N. Ullah, J. Ahmad, F. Sikandar, M.M. Ehsan, S. Salehin, A.A. Bhuiyan, Heat transfer and pressure drop performance of nanofluid: a state-of-the-art review, Int. J. Thermofluids 9 (2021), 100065.

[59] Y. Zhu, Y. Chi, S. Liang, X. Luo, K. Chen, C. Tian, L. Zhang, Novel metal coated nanoencapsulated phase change materials with high thermal conductivity for thermal energy storage, Sol. Energy Mater. Sol. Cells 176 (2018) 212–221.

[60] R.R. Sahoo, V. Kumar, Development of a new correlation to determine the viscosity of ternary hybrid nanofluid, Int. Commun. Heat Mass Transf. 111 (2020), 104451.

[61] M.H. Esfe, A.A.A. Arani, M. Rezaie, W.M. Yan, A. Karimipour, Experimental determination of thermal conductivity and dynamic viscosity of Ag–MgO/water hybrid nanofluid, Int. Commun. Heat Mass Transf. 66 (2015) 189–195.